Title:

Mechanistic insight into substrate processing and allosteric inhibition of human p97

Authors:

Man Pan,[1,3,*] Yuanyuan Yu,[1,3] Huasong Ai,[2] Qingyun Zheng,[2] Yuan Xie,[1] Lei Liu,[2,*] Minglei Zhao[1,*]

Affiliations:

[1] Department of Biochemistry and Molecular Biology, The University of Chicago; Chicago, IL 60637, USA.

[2] Tsinghua-Peking Center for Life Sciences, Department of Chemistry, Tsinghua University; Beijing 100084, China.

[3]These authors contributed equally to the work.

*Corresponding authors:

Minglei Zhao. Email: mlzhao@uchicago.edu

Lei Liu. Email: lliu@mail.tsinghua.edu.cn

Man Pan. Email: panm@uchicago.edu

Abstract:

p97 processes ubiquitinated substrates and plays a central role in cellular protein homeostasis. Previous studies have showed that it is a potential drug target for cancer, neurodegenerative disease, and viral infections. Here, we report a series of cryo-electron microscopy (cryo-EM) structures of substrate-engaged human p97 complex that captured “power stroke”-like motions of both the D1 and D2 ATPase rings of p97. A key feature of these structures is the critical conformational changes of the inter-subunit signaling (ISS) motifs, which tightens the binding of nucleotides and neighboring subunits, and contributes to the spiral staircase conformation of the D1 and D2 rings. We further determined the cryo-EM structure of human p97 in complex with NMS-873, the most potent p97 inhibitor. The structures showed that NMS-873 binds at a cryptic groove in the D2 domain and interacts with the ISS motif, preventing its conformational change, thus blocking substrate translocation allosterically.

Keywords

p97, NMS-873, single-particle cryo-EM, translocation, allosteric inhibition

39 **INTRODUCTION**

40 p97 is a 540 kDa protein that belongs to the family of ATPases Associated with diverse
41 cellular Activities (AAA)[1-3]. It undergoes repetitive ATP hydrolysis and conformational changes
42 to extract ubiquitinated substrates from various cellular components, such as membranes,
43 ribosomes, and chromatin[4]. p97 plays a central role in many cellular processes, including
44 endoplasmic reticulum-associated degradation (ERAD), mitochondrial-associated degradation,
45 chromatin-associated degradation, autophagy, and endosomal trafficking[5]. Mutations in human
46 p97 have been found in multisystem proteinopathy (MSP), a dominantly inherited degenerative
47 disorder that can affect muscle, bone and the central nervous system, that can manifest
48 clinically as inclusion body myopathy with early-onset Paget disease and frontotemporal
49 dementia (IBMPFD) and familial amyotrophic lateral sclerosis (ALS)[6,7]. Moreover, recent studies
50 have also targeted p97 for the treatment of cancer and viral infections[8,9].

51 p97 has two tandem AAA domains named D1 and D2 and an additional N domain at the
52 N-terminus (**Fig. 1a**). This protein functions as a homomeric hexamer, with twelve copies of
53 ATPase domains organized into two rings[10]. Crystal structures of full-length p97 were
54 determined more than a decade ago[11,12]. High-resolution single-particle cryo-electron
55 microscopy (cryo-EM) structures have also been reported[13,14]. However, all the structures of p97
56 determined thus far adopt a sixfold symmetric conformation, providing limited information
57 regarding the mechanism since almost all AAA proteins, including close homologues of p97,
58 break symmetry when engaged with substrates[15-17]. Recent cryo-EM studies of Cdc48, the
59 yeast homolog of p97, in complex with either in vivo[18] or in vitro[19] substrates provided crucial
60 insight into the working states. However, with medium resolution (3.7 Å to 4.2 Å) and limited
61 conformational states, critical mechanistic questions, such as how the AAA domains in two rings
62 coordinate to achieve translocation, remain to be answered. In addition, owing to its biomedical
63 importance, many small-molecule inhibitors of p97 have been developed in the past
64 decade[8,20,21]. NMS-873, a non-competitive allosteric inhibitor of p97[21], has been shown to be

active in tumor cell lines and IBMPFD patient fibroblasts[21,22]. More importantly, low nanomolar concentrations of NMS-873 was recently reported to inhibit the replication of several viruses, including severe acute respiratory syndrome coronavirus 2 (SARS-CoV-2) and influenza virus, through its inhibition of p97[23-25]. Little is known regarding the allosteric inhibition mechanism due to the lack of a substrates-engaged human p97 structure in a working state, which is of considerable biological and clinical interest.

In this study, starting from a fully assembled human p97 complex with the cofactor Npl4/Ufd1 and a substrate, we triggered ATP hydrolysis and determined a series of substrate-engaged p97 structures with resolutions ranging from 2.9 to 3.8 Å using single-particle cryo-EM. The structures captured ATP hydrolysis driven “power stroke”-like motions of both the D1 and D2 rings of p97 and elucidated how the two rings coordinate to achieve translocation through inter-subunit signaling (ISS) motifs, the pore loops, and N- and C-terminal tails. We further determined the cryo-EM structure of p97 in the presence of NMS-873 at a resolution of 2.4 Å and uncovered a novel inhibition mechanism. Finally, using NMS-873 at a substoichiometric concentration, we captured a series of intermediate states, suggesting how p97 coordinates with its cofactor Npl4 to initiate substrate translocation. Taken together, our results established a comprehensive understanding of substrate processing and allosteric inhibition of human p97.

RESULTS

Capture the working states of human p97

First, we assembled complexes of p97 from recombinantly overexpressed components without introducing additional ATP. Two mutations, A232E and E578Q, were introduced into the human p97 construct to stabilize the complex as previously described [26]. The A232E mutation has been found in MSP patients and has been reported as an activating mutant with its N domains shifted toward the “up conformation” [27]. E578Q is a mutation in the Walker B motif of the D2 domain that slows substrate unfolding[19,28]. Combined, the two mutations decreased but maintained the unfolding activity of p97 (**Extended Data Fig. 1a**) and minimized the conformational heterogeneity resulting from the N domains. All the structural work in this study used the p97 (A232E/E578Q) mutant and Npl4/Ufd1 as the cofactors. For substrates, either polyubiquitinated Ub-Eos (Ub_n-Eos) or K48-linked hexa-ubiquitin (Ub_6) was used. The assembled complex, named p97-Npl4/Ufd1-Ub_n-Eos or p97-Npl4/Ufd1-Ub_6, eluted as single peaks in the size-exclusion chromatograms (**Extended Data Fig. 1b and c**). To capture the working states of p97, ATP hydrolysis was triggered by adding 5 mM ATP to the purified complexes followed by incubation at room temperature for 5 minutes. To solve the orientation preference problem to the greatest extent, either CHAPSO or fluorinated octyl maltoside (FOM) was added immediately before sample vitrification (**Fig. 1b**). Three datasets, namely, p97-Npl4/Ufd1-Ub_n-Eos-CHAPSO, p97-Npl4/Ufd1-Ub_n-Eos-FOM, and p97-Npl4/Ufd1-Ub_6-FOM, were collected, and a total of 9 different cryo-EM maps with resolutions ranging from 2.9 to 3.8 Å were reconstructed using single-particle analysis (**Extended Data Fig. 2-4, Supplementary Table 1**). Atomic models were built based on existing p97 structures (**Supplementary Table 2**). For well-resolved regions, individual residues were manually built into the density. For flexible regions, rigid body docking was used to fit individual secondary structure elements or subdomains (see Methods for details).

109 **Open and closed states of the D2 ring**

110 In the p97-Npl4/Ufd1-Ub_n-Eos-CHAPSO dataset, two conformational states of the D2
111 ring were resolved (**Fig. 1c and d**). In the open state (3.6 Å, **Fig. 1c**, corresponding to class 2
112 in **Extended Data Fig. 2**), all six D2 domains interacted with the substrate and formed an open,
113 right-handed spiral staircase, whereas in the closed state (3.1 Å, **Fig. 1d**, corresponding to
114 class 1 in **Extended Data Fig. 2**), the bottom D2 domain (termed chain F) detached from the
115 substrate and shifted up to interact with the top D2 domain (termed chain E), closing the gap of
116 the spiral in the open state. Only five D2 domains (chains A-E) interacted with the substrate in
117 the closed state. The two states suggested a "power stroke"-like motion of the D2 domain
118 (**Supplementary Movie 1**). Compared to the same complex structure in the presence of ATPγS
119 that was previously published[26] (PDB ID: 7JY5), there was a relative 20 degree rotation of the
120 D2 ring to the D1 ring in both states (**Fig. 1e and Extended Data Fig. 6a**). A superimposition of
121 the two states showed that the D2 domain immediately above chain F (chain A) also shifted up
122 from the open state to the closed state (**Extended Data Fig. 7a** and **Supplementary Movie 1**).
123 The particles in the open state were significantly less than those in the closed state (13% vs.
124 70%), suggesting that the open state is relatively transient. A third class was resolved from the
125 3D classification (3.8 Å, class 3 in **Extended Data Fig. 2**), with better resolved density for the
126 cofactor Npl4 but otherwise the same conformation as the closed state.

127

128 **Conformational changes in the D1 ring**

129 In the p97-Npl4/Ufd1-Ub_n-Eos-FOM dataset, three conformational states of the D1 ring
130 were resolved (**Extended Data Fig. 3**). All the D2 rings were in the same conformation as the
131 closed state described above. Using the same naming convention, we discovered from the
132 superimposed structures that chain A shifted up slightly from class 1 (3.6 Å) to class 2 (3.4 Å)
133 and much further from class 2 to class 3 (3.0 Å) (**Extended Data Fig. 8a**). No open spiral
134 conformation similar to the open state of the D2 ring was observed for the D1 ring, although a

135 right-handed spiral staircase was still formed by chains B-F. The three states of the D1 ring also
136 suggested a “power stroke”-like motion despite the differences from the D2 ring
137 (**Supplementary Movie 2**). It is worth noting that no conformational changes in the D1 ring
138 were observed for the p97-Npl4/Ufd1-Ub_n-Eos-CHAPSO dataset. The conformation of the D1
139 ring in the open and closed states was very similar to class 3 of the p97-Npl4/Ufd1-Ub_n-Eos-
140 FOM dataset (see Discussion).
141
142 **Sequential but asynchronous hydrolysis in D1 and D2 rings**
143 The resolutions of the maps allowed us to build atomic models and identify the
144 nucleotides in most nucleotide binding sites (**Extended Data Fig. 7d and S8d**). For the less
145 well resolved chains A and F, the identity of the nucleotides could not be determined with
146 certainty, but the density of a nucleotide was clearly visible (**Extended Data Fig. 7d and S8d**).
147 All nucleotide binding sites were occupied, suggesting that the nucleotide exchange might be
148 very fast. When superimposing all the AAA domains within the same ring, two major
149 conformations were observed: one with a larger angle between the α/β and the α subdomain,
150 potentially corresponding to an ATP binding conformation, and the other with a smaller angle
151 between the α/β and the α subdomain, potentially corresponding to an ADP binding
152 conformation (**Extended Data Fig. 7c and 8c**). Such binary conformations have been
153 observed for other substrate-engaged AAA+ structures [15-19,29,30].
154 When focusing on the well-resolved sites, we discovered a new compact ATP binding
155 mode in both the D1 and D2 rings involving a previously defined ISS motif[31]. Specifically, the
156 ISS motif changed from a helical conformation to a triangular loop that inserted into the
157 neighboring nucleotide binding site (**Fig. 1e and f**), and these conformational changes were
158 closely related to the spiral staircases formed by the pore loops (**Fig. 2a and Extended Data**
159 **Fig. 5a and b)**. L335 in the D1 domain and M611 in the D2 domain are the key residues
160 interacting with the hydrophobic residues in the Walker B motifs of the neighboring subunits

161 (**Fig. 1f**). As a result, ATP is coordinated by three more residues than the ATPγS-bound
162 structure (PDB ID: 7JY5), including one additional arginine finger residue (R362 in D1 and R638
163 in D2), an aspartic acid from the ISS motif (D333 in D1 and D609 in D2), and a basic residue
164 following the Walker A motif (R256 in D1 and K529 in D2) (**Fig. 1f**). This binding mode was
165 observed only when ATP was engaged and only for two to four consecutive binding sites in both
166 rings (**Fig. 1e**, **Extended Data Fig. 7b and S8b**). We hypothesize that this tight binding mode
167 is required for the formation of spiral staircases and the rotational compression of ATPase rings,
168 both essential for substrate translocation. For ATP hydrolysis or ADP release to occur, the ISS
169 motif needs to be retracted to loosen the binding with the nucleotide. For example, the ISS motif
170 in the D2 domain of chain A retracted in the closed state (not in the open state) since the
171 neighboring D2 domain in chain B is the next subunit to undergo ATP hydrolysis or ADP release
172 (**Fig. 1e and Extended Data Fig. 7b**).
173 Another unexpected observation is that the hydrolysis in the D1 and D2 rings is not in
174 sync, which means that at a given time, the D1 and D2 domains of the same chain may engage
175 different nucleotides. If viewed from the top, hydrolysis propagates counterclockwise in both
176 ATPase rings, with the D1 ring one or two subunits ahead of the D2 ring (**Fig. 1e**). This feature
177 is unique for human p97 and has not been observed for other type II AAA proteins, including
178 yeast Cdc48.
179
180 **Interactions between the pore loops and the substrate**
181 In all six maps discussed above, we observed the density corresponding to a
182 translocating peptide going through the central pore of p97 (**Fig. 2b**). A continuous extended
183 peptide could be modeled into the density. The peptide went through the pore from the N-
184 terminus (bottom in **Fig. 2b**) to the C-terminus (top in **Fig. 2b**), as the other direction fit much
185 worse into the density. This directionality of translocating peptide is consistent with that of

186 Cdc48[18,19]. The density corresponding to the side chains was averaged, and polyalanine was
187 modeled.

188 In general, the density of the translocating peptide in the D2 ring was better than that in
189 the D1 ring. Three residues in pore loop-I (PL-I) of the D2 domain, namely, M550, W551, and
190 F552, interacted with the peptide like a “pitching grip” (**Fig. 2b**). Each PL-I formed two hydrogen
191 bonds with the nitrogen and carbonyl oxygen of one residue in the translocating peptide through
192 the carbonyl oxygen of M550 and nitrogen of F552. Every other residue in the translocating
193 peptide was hydrogen bonded by a PL-I so 12 residues were engaged with six PL-I in the D2
194 ring, which formed a spiral in the open state, with chain F at the bottom and chain E at the top
195 (**Fig. 2b**). In the closed state, the PL-I of chain F detached from the translocating peptide. The
196 remaining five PL-I formed the spiral in a very similar way except for the side chain of M550 in
197 chain A (now the bottom chain), which was pointing downwards and would not allow an
198 additional PL-I to engage (**Fig. 2b inset**). In both the open and closed states, the density of five
199 pore loop-II (PL-II) in the D2 ring was resolved (chains A to E) but at lower resolution (**Fig. 2b**
200 **inset**). PL-II in the D2 ring did not form hydrogen bonds with the translocating peptide and likely
201 played a less important role in translocation. We mutated the residues of PL-I and PL-II and
202 performed the substrate unfolding assay[1,26,32]. Indeed, the PL-I mutation (W551A/F552A)
203 abolished the unfolding activity, whereas the PL-II mutation (I590A/D592A) showed no effect
204 (**Fig. 2e**). A closer examination revealed that R599 was π-stacked with F552 of PL-I (**Fig. 2c**).
205 This interaction might be critical to stabilize the “pitching grip” conformation of PL-I since the
206 R599A mutant did not show any unfolding activity, similar to the PL-I mutation (**Fig. 2e**). In
207 contrast, the pore loops in the D2 domain of the nontranslocating structure (PDB ID: 7JY5) were
208 mostly unstructured (**Fig. 2d**).

209 PL-I in the D1 ring interreacted with the translocating peptide in the same fashion as that
210 in the D2 ring, except that only four PL-I (chains B-E) were engaged and the three residues
211 were K277, L278, and A279 (**Fig. 2b**). The “pitching grip” and hydrogen bonding pattern still

212 existed, but the interaction was not as strong as that of the D2 ring since the average length of
213 the hydrogen bonds was 3.9 Å in the D1 ring and 3.4 Å in the D2 ring. Two PL-II of the D1 ring
214 (chains C and D) were involved in the interaction with the peptide by forming a hydrogen bond
215 through H317 (**Fig. 2b**). Interestingly, H317 of chains B and C also stacked with W551 (PL-I of
216 D2) of chains D and E, respectively (**Fig. 2b**, red double arrow). This π-π stacking might be
217 involved in the coordination of two ATPase rings.

218 To further investigate the behavior of p97 with substrates of different sizes, we used a
219 much smaller substrate, Ub_6 (**Extended Data Fig. 1c**), and collected a third dataset, p97-
220 Npl4/Ufd1-Ub_6-FOM (**Extended Data Fig. 4**). Again, three conformations of the D1 ring that
221 were very similar to those of the p97-Npl4/Ufd1-Ub_n-Eos-FOM dataset were resolved.
222 Intriguingly, the density corresponding to the translocating peptide was resolved only in the D2
223 ring (**Fig. 2f**). The D1 ring was essentially void of the translocating peptide despite adopting the
224 same conformation. One possible explanation is that the D1 ring is engaged only when a
225 "complicated" substrate such as Ub_n-Eos is encountered.

226 We noticed that the D2 ring of the closed state is similar to those of Cdc48-ADP·BeFx
227 structures [18,19], all of which have five PL-I engaging with the translocating peptide. When the D2
228 rings from these structures were superimposed, it was obvious that the two rings of p97 are out
229 of register, that is, the lowest D2 and D1 domains are not in the same chain (**Fig. 2g and**
230 **Extended Data Fig. 5c**), whereas in Cdc48, the two rings essentially formed a single "split
231 washer" (**Fig. 2h and Extended Data Fig. 5d**). Accordingly, the entire chain F (named based
232 on Fig. 1) is flexible in previous Cdc48-ADP·BeFx structures, whereas in our structures the D2
233 domain of chain F and the D1 domain of chain A are the most flexible. These features are
234 consistent with the asynchronous hydrolysis occurring in the D1 and D2 rings.
235

236 **N- and C-terminal tails and the linker between D1 and D2 rings**

237 In addition to the ATPase rings, some of the N- and C-terminal tails (**Fig. 1a**) of p97
238 were also resolved in the cryo-EM maps. Both the resolved N-terminal (L12 to R22) and C-
239 terminal (G767-S775) tails interacted with the neighboring subunit in a counterclockwise manner
240 if viewed from the top (N-terminal tail, **Fig. 3a**) or a clockwise manner if viewed from the bottom
241 (C-terminal tail, **Fig. 3c**). The N-terminal tail interacted with an acidic patch in the α subunit of
242 the D1 domain (**Fig. 3b**). The C-terminal tail interacted with a groove in the α subunit of the D2
243 domain. Such interactions have not been described before and may play important roles in the
244 coordination between different chains. Truncations of either the N- or C-terminal tails greatly
245 affected the unfolding activity of p97 (**Fig. 3f**). The linker between the D1 and D2 rings was
246 resolved for chains B-E. Compared to the structure of nontranslocating p97 (PDB ID: 7JY5), a
247 19 Å shift of L464 was observed (**Fig. 3e**). In the translocating structure, L464 interacted with
248 A569 in the D2 domain, which contributed to the relative twist of the D2 ring (**Fig. 1e**). The
249 L464A mutation decreased the unfolding activity of p97 (**Fig. 3f**). Notably, the N- and C-
250 terminal tails and the linker regions are less conserved between human p97 and yeast Cdc48,
251 which might contribute to the different conformations of the ATPase rings.
252
253 **NMS-873 inhibits the translocation by locking the ISS motif**
254 Inhibition of p97 has emerged as a promising strategy in anticancer and antiviral
255 studies[8]. NMS-873, the first discovered allosteric inhibitor of p97 (**Fig. 4a**), was recently
256 characterized as a candidate for the treatment of cancers, neurodegenerative diseases, and
257 viral infections[22-24]. However, the mechanism of inhibition remained unclear. We introduced
258 NMS-873 at saturation (80 μM) after triggering ATP hydrolysis and substrate translocation (**Fig.
259 4b**). Two datasets were collected using Ub_n-Eos and Ub_6 as the substrate. A single map was
260 obtained from each dataset with overall resolutions of 2.4 Å (Ub_6, **Extended Data Fig. 9**) and
261 2.8 Å (Ub_n-Eos, **Extended Data Fig. 10**). The two maps are essentially identical; therefore, only
262 the map with the higher resolution is shown (**Fig. 4c**). Unexpectedly, both maps showed that

263 p97 maintained 6-fold symmetry and no translocating peptides were found in the central pore,
264 although a substrate was present and ATP hydrolysis was triggered before adding NMS-873. In
265 the 6-fold symmetric structure of p97, NMS-873 binds at a cryptic groove next to the ISS motif of
266 the D2 domain (**Fig. 4d**) and is surrounded by many hydrophobic residues (**Fig. 4e**). A critical
267 interaction was observed between K615 in the ISS motif and the biphenyl group of NMS-873
268 (**Fig. 4d**). As a result, the ISS motif is locked and prevented from essential conformational
269 changes discovered in the translocating structures (**Fig. 4f**). The pore loops in the D2 domain
270 of the NMS-873-bound structure were resolved but retracted from the pore compared to the
271 translocating structure (**Extended Data Fig. 6e**). Together, these structural features make it
272 impossible to form a spiral staircase by the PL-1 of D2 ring, which might explain why no
273 translocating peptide was found in the pore.

274 Compared to the ATPγS-bound nontranslocating structure (PDB ID: 7JY5), the relative
275 positions of the ATPase rings in the NMS-873-bound structure are similar (**Extended Data Fig.**
276 **6b**). The difference is that the bottom opening of the D2 ring is enlarged, which is similar to that
277 of the ADP-bound structures[13], although ATP was engaged (**Extended Data Fig. 6c**). The
278 smaller angle between the α/β and the α subdomains of the D2 domains suggested that it is
279 more similar to an ADP-bound state, indicating that NMS-873 can affect the conformation of the
280 D2 ring regardless of the nucleotide states (**Extended Data Fig. 6d**). Superimposing the NMS-
281 873-bound structure with another inhibitor-bound structure (UPCDC30245, PDB ID: 5FTJ [13])
282 showed the similarity in the conformations of pore loops. The difference is that UPCDC30245
283 only shares part of the binding pocket of NMS-873 in the D2 domain (**Extended Data Fig. 6f**
284 **and S6g**). Especially, the interaction between K615 and the biphenyl group of NMS-873 does
285 not occur in the UPCDC30245-bound structure (**Fig. 4f and Extended Data Fig. 6g**), which
286 was also reported from previous biochemical characterizations [13,21]. Combined with previous
287 finding that UPCDC30245 binds p97 only in the presence of ADP and acts as an uncompetitive
288 inhibitor, whereas NMS-873 can bind p97 in the absence of nucleotides and acts as a

289 noncompetitive inhibitor [8], we concluded that the ISS-locking mechanism of NMS-873 through
290 the interaction with K615 is the key to the non-competitive allosteric inhibition.
291
292 **Conformational states of Npl4 revealed by NMS-873 at a substoichiometric concentration**
293 We further discovered that NMS-873 did not fully inhibit the unfolding activity of p97 at a
294 substoichiometric concentration (6 equivalents (eq) is the stoichiometric concentration, **Fig.**
295 **4g**). On the reasoning that intermediate structures could be captured using NMS-873 as a
296 modulator, a dataset was collected following the same protocol using Ub_n-Eos as the substrate
297 and in the presence of 10 μM NMS-873 (~0.2 eq, **Fig. 5a**). As expected, multiple intermediate
298 structures were resolved after 3D classification (**Extended Data Fig. 11**). Two out of six maps
299 (~11% particles) are in the nontranslocating state, with flat and symmetric ATPase rings and no
300 density for a translocating peptide (**Fig. 6c**). One of the nontranslocating maps (Class 1, ~8%
301 particles) showed the density of NMS-873 (**Fig. 6c**, top) in all six binding pockets, suggesting
302 that the binding of NMS-873 is highly cooperative. The cofactor Npl4 was resolved in four out of
303 six maps (**Extended Data Fig. 11**). Both nontranslocating maps showed density for Npl4, with
304 either one or two of its zinc finger motifs (ZF1 and ZF2, **Fig. 5b**) binding on top of the D1 ring
305 (**Fig. 6c**). Such seesaw conformations of Npl4 have been described in a previous study[26]. The
306 four translocating structures all had spiral ATPase rings and a translocating peptide similar to
307 the conformation of the closed state (**Extended Data Fig. 11**). Two maps (class 5 and class 6)
308 had very poor densities of Npl4 and differed in the D1 ring in a similar way to class 1 and class 3
309 of the p97-Npl4/Ufd1-Ub_n-Eos-FOM dataset. The other two maps showed density for Npl4, but
310 with its zinc finger motifs interacting with different chains (**Fig. 6d**), suggesting a rotation of
311 Npl4 on top of the D1 ring. Although the resolution of Npl4 is not sufficient for atomic model
312 building, a trace density connected to the translocating peptide can be seen to be engaged in a
313 groove of Npl4 (**Fig. 6d**, top), which is reminiscent of a substrate processing complex structure
314 of Cdc48[19].

316 **DISCUSSION**

317 Here, we report the cryo-EM structures of human p97 in several working states, with a
318 translocating peptide going through the central pore. Together, the structures revealed "power
319 stroke"-like conformational changes in both the D1 and D2 rings. Surprisingly, the two AAA
320 domains undergoing power stroke motion in each ring were not from the same chain, which
321 seemed to be a unique feature of human p97 and was not observed for Cdc48 and other Type-II
322 AAA proteins[15,16,18,19,29,30]. The unusual structural feature corresponds to the asynchronous
323 hydrolysis taking place in the two ATPase rings (**Fig. 1e and Extended Data Fig. 5c and d**).
324 Regarding translocation, the D2 ring seemed to play a more important role by tightly interacting
325 with the peptide through backbone hydrogen bonds. Previous biochemical studies have shown
326 that the D2 ring of p97 had higher ATPase activity and provided the driving force for
327 translocation, which is consistent with our structures[33]. The structures of Cdc48 also showed
328 fewer interactions between the translocating peptide and the pore loops of the D1 ring[19], further
329 supporting this hypothesis. Regarding the role of the D1 ring in substrate translocation, we
330 obtained some insights from the datasets using Ub_n-Eos and Ub_6 as the substrate, respectively.
331 In the translocating structures with Ub_n-Eos, peptide density was observed in both D1 and D2
332 rings, while in the structures with Ub_6, the peptide density was only observed in the D2 ring.
333 Therefore, D1 ring may be engaged when larger substrate proteins are encountered.

334 Although the structures strongly support a sequential hydrolysis model[34], it is not clear
335 whether the power strokes in the D1 and D2 rings take place concurrently. Multiple structures
336 from a single dataset are needed to address this question. In this study, the motions of the D1
337 and D2 rings were resolved from two datasets, one using CHAPSO and the other using FOM as
338 the detergent to fix the orientation preference. CHAPSO required a much higher concentration
339 of the complex than FOM (8x) to keep the samples in the hole but seemed to preserve the
340 complex better and yielded more particles with Npl4. Since the open state is a minor

341 conformation (7% of the total particles, **Extended Data Fig. 2**), the higher concentration of the
342 CHAPSO dataset may have contributed to its discovery.
343 One critical finding in this study is the conformational changes of the ISS motifs in both
344 ATPase rings in the translocating structures (**Figs. 1F, 2a and Extended Data Fig. 5a-b**).
345 Structures of human p97 in the presence of NMS-873 revealed the allosteric inhibition
346 mechanism that NMS-873 binds and locks the ISS motifs in the D2 ring to prevent
347 conformational changes (**Figs. 4d-f**), which further affects the pore loops and prevents
348 substrate translocation. Targeting the ISS motif of p97, therefore, may serve as a potential
349 strategy for the development of new inhibitors.
350 Multiple structures in the presence of NMS-873 at a substoichiometric concentration
351 suggested that Npl4 may play a critical role in the initiation of translocation by unfolding the
352 ubiquitin chain and threading it into the central pore through a seesaw motion. The pore loops in
353 the D1 and D2 rings catch the thread-in peptide, and the two rings are compressed to spiral
354 conformations. Following sequential ATP hydrolysis and power stroke motions circulating in
355 both rings, the peptide in the pore is translocated downward. Npl4 might be unnecessary once
356 the translocation starts.
357 Mutations in p97 have been linked to MSP[6,35]. Structures of p97 in working states
358 provided crucial insights into the consequences of the mutations (**Supplementary Table 3,**
359 **Supplementary Movie 3**). The resolutions of the cryo-EM maps in this study are among the
360 highest of type II AAA proteins[15,17,19,30,36], allowing a comprehensive understanding of substrate
361 processing and allosteric inhibition of human p97 and shedding light on the mechanism of other
362 type II AAA proteins.
363

ACKNOWLEDGEMENTS

We thank staff at the National Cryo-Electron Microscopy Facility at the Frederick National Laboratory and the Advanced Electron Microscopy Facility at the University of Chicago for the help in cryo-EM data collection. **Funding:** Funding for this work was, in part, provided by the Catalyst Award from the Chicago Biomedical Consortium**.** This work was supported by Chicago Biomedical Consortium Catalyst Award C-086 to M.Z. We thank the National Key R&D Program of China (No. 2017YFA0505200), NSFC (91753205) for financial support. This research was, in part, supported by the National Cancer Institute's National Cryo-EM Facility at the Frederick National Laboratory for Cancer Research under contract HSSN261200800001E.

AUTHOR CONTRIBUTIONS

M.P., M.Z. and L.L. designed all the experiments and interpreted the results. M.P., Y.Y., H.A., Q.Z., and Y.X. cloned, expressed, and purified all the complexes and carried out related biochemical characterizations. M.P., Y.Y., and M.Z. performed cryo-EM data collection and processing. M.Z., M.P., and L.L. wrote the paper. M.Z., L.L., and M.P. supervised the project.

COMPETING INTERESTS

The authors declare no competing interests.

384 **Figure Legends**

385 **FIG. 1**

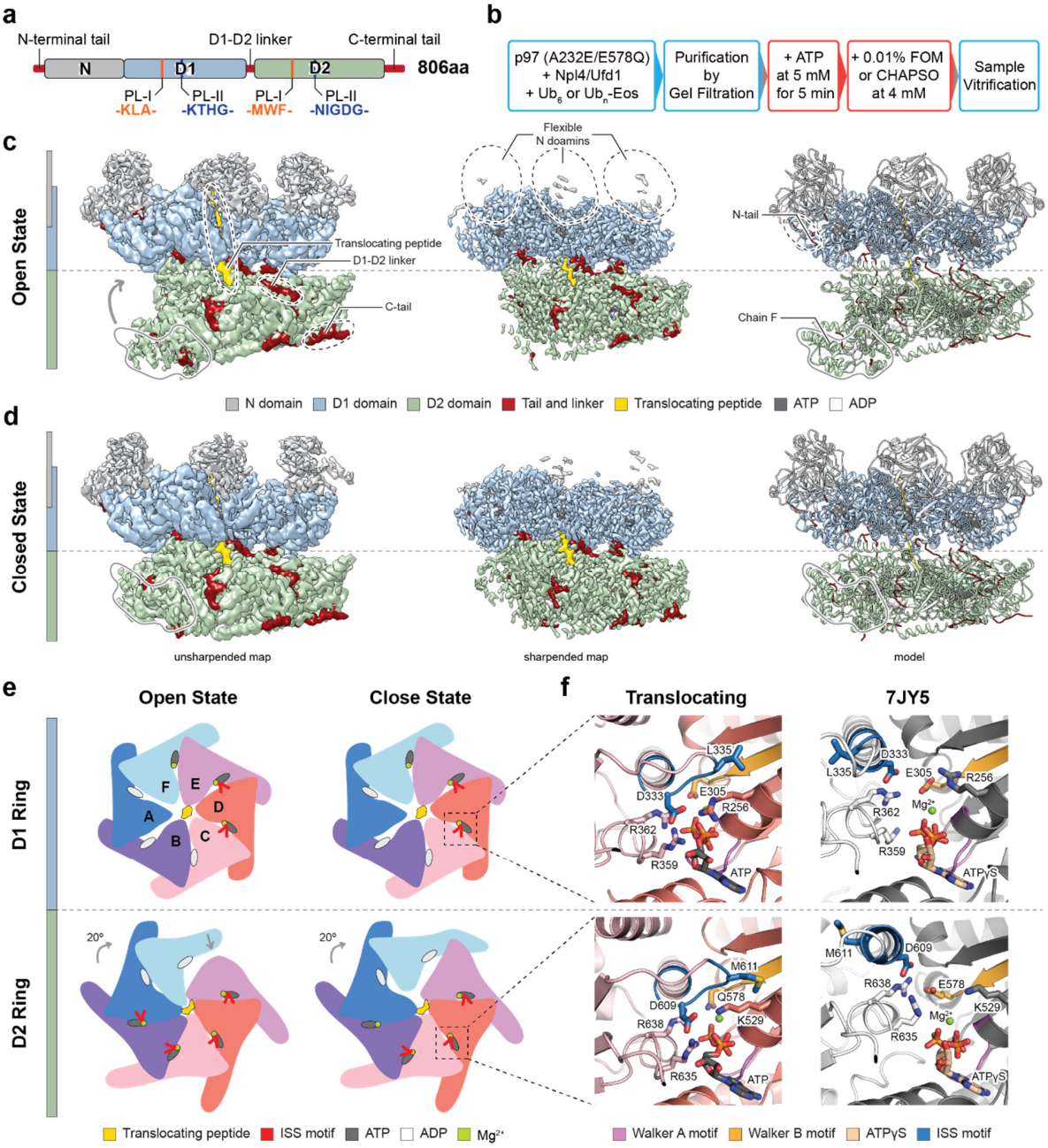

386

387 **Fig. 1: Structures of human p97 in working states.**

388 **a,** Domain architecture of human p97. The color code of individual domains is used whenever

389 possible. Pore loop residues in D1 and D2 domains are listed. **b,** Sample preparation

procedures. Steps performed at 4 °C are in blue boxes. Steps performed at room temperature are in red boxes. **c** and **d,** Cryo-EM maps and models of human p97 engaged with a translocating peptide. The maps and models are aligned. Contour level: unsharpened map, 0.015; sharpened map, 0.035. **c,** Open state. **d,** Closed state. **e,** Illustrations showing the arrangement of the D1 and D2 rings in the open and closed states, respectively. **f,** Magnified views of compressed ATP binding sites in the D1 and D2 rings. The corresponding ATPγS binding sites from the nontranslocating structure (PDB ID: 7JY5) are shown for comparison.

398 **FIG. 2**

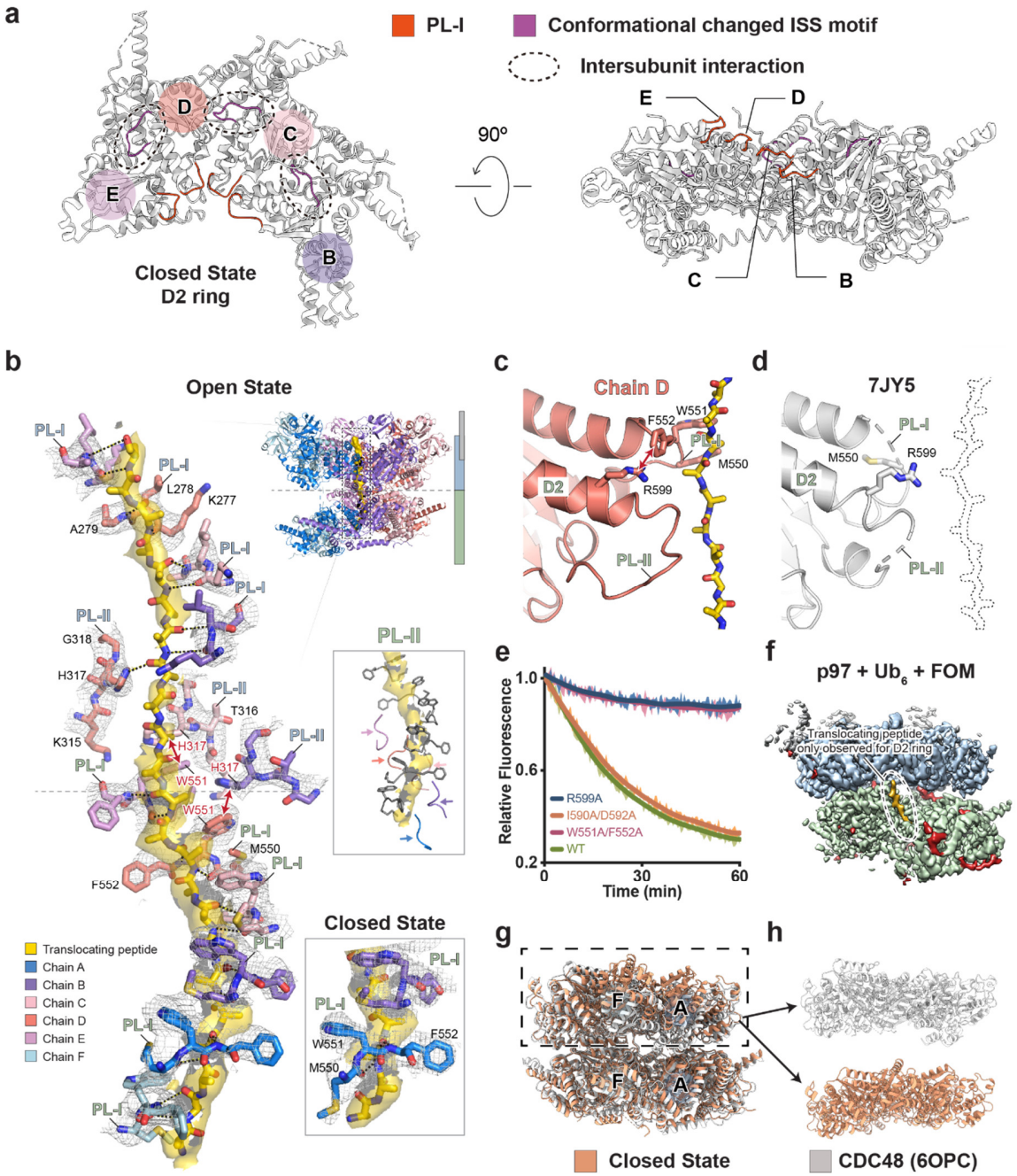

399

400 **Fig. 2: Interactions between the pore loops and the substrate.**

401 **a,** Illustrations showing the arrangement of chains B-E in the D2 ring of the closed state. **b,**

402 Interactions between the translocating peptide and the interacting pore loops in the D1 and D2

403 rings. The density of the pore loops and the translocating peptide are shown as a gray mesh

404 and yellow surface, respectively. Contour level: 6.0 root-mean-square deviation (rmsd). The
405 closed state and PL-II of the D2 ring are shown in the insets. Hydrogen bonds between the pore
406 loops and the peptide are labeled with black dotted lines. π-π interactions between H317 and
407 W551 are labeled with red double arrows. **c and d,** A comparison of the D2 domain in chain D
408 of the open state (panel **c**) and that of the nontranslocating structure (panel **d**, PDB ID: 7JY5).
409 The D2 domains are aligned. **e,** Substrate unfolding assay for the pore loop mutants of p97. The
410 error bands represent the standard deviation from triplicate experiments. **f,** Unsharpened cryo-
411 EM map (class 1) of the p97-Npl4/Ufd1-Ub_6-FOM dataset (**Extended Data Fig. 4**). The map is
412 shown in a similar orientation to **Fig. 1d and 1e**. Contour level: 0.015. **g**, A comparison of cryo-
413 EM models of translocating structures of p97 (closed state, orange) and Cdc48 (PDB ID: 6OPC,
414 light grey). The two models were aligned based on the D2 ring. **h**, A close view of the D1 rings
415 in panel **g**.
416

417 **FIG. 3**

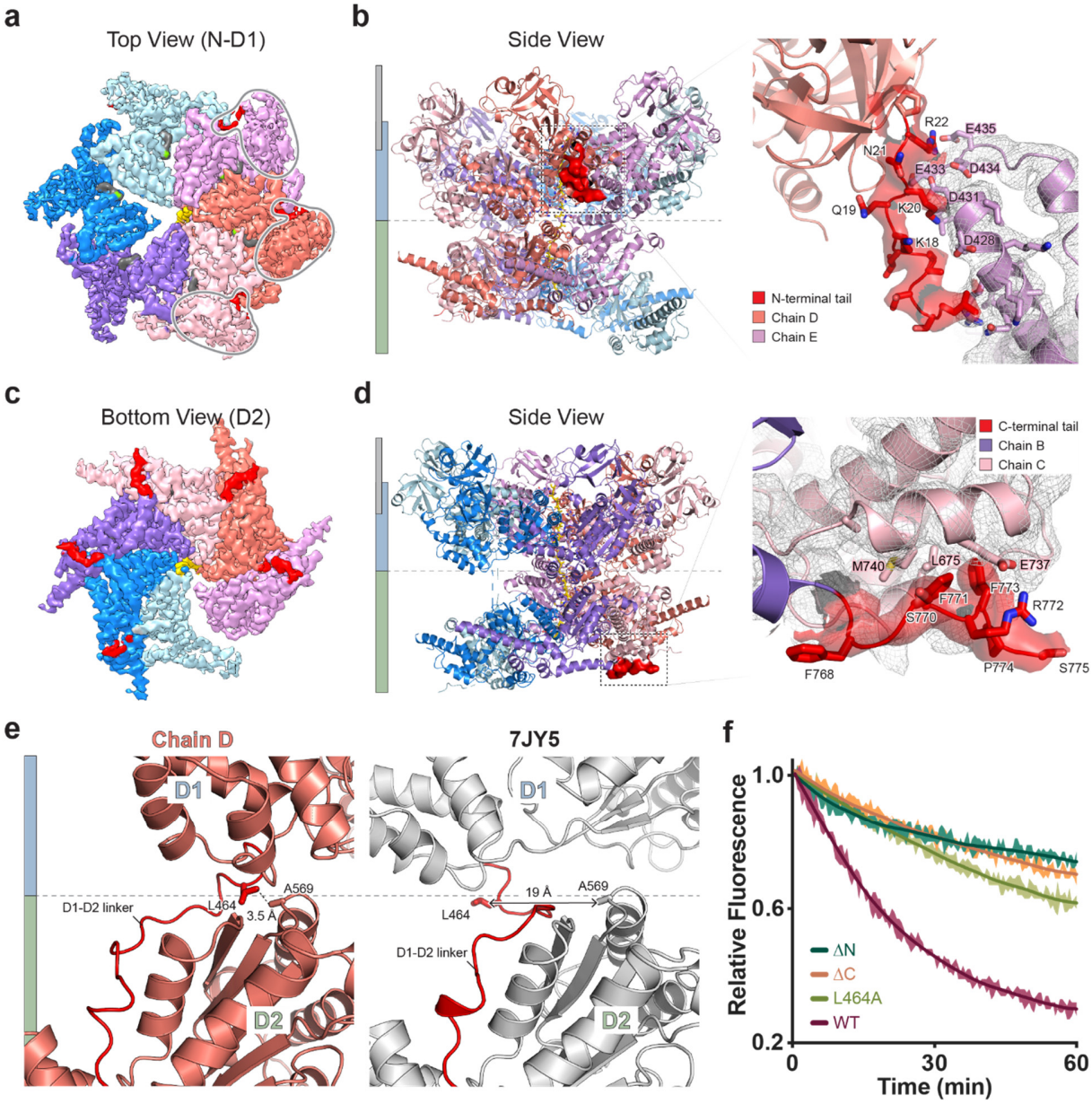

418

419 **Fig. 3: N- and C-terminal tails and the linker between the D1 and D2 rings.**

420 **a,** Top view of the unsharpened cryo-EM map focused on the N and D1 domains (open state).

421 N-terminal tails are colored in red. Contour level: 0.015. **b,** A side view of the cryo-EM model of

422 the open state with the density of one N-terminal tail highlighted and magnified. Contour level:

423 6.0 rmsd. **c,** A bottom view of the unsharpened cryo-EM map focused on the D2 ring (open

state). C-terminal tails are shown in red. Contour level: 0.015. **d,** A side view of the cryo-EM model of the open state with the density of one C-terminal tail highlighted and magnified. Contour level: 6.0 rmsd. **e,** A comparison of the D1-D2 linker in chain D of the open state and that of the nontranslocating structure (PDB ID: 7JY5). The D2 domains are aligned. **f,** Substrate unfolding assay for tail and linker mutants of p97. The error bands represent the standard deviation from triplicate experiments.

431 **FIG. 4**

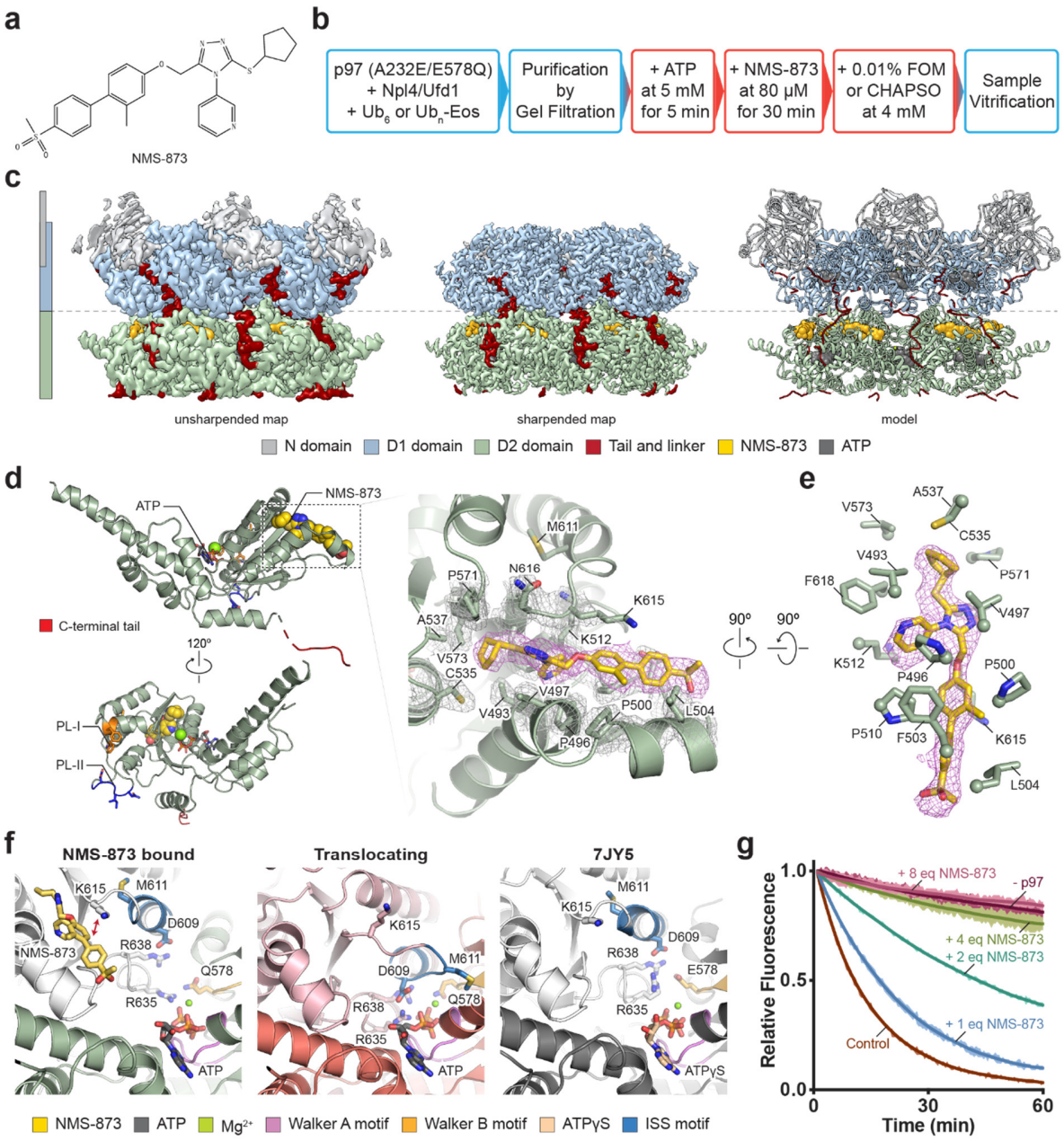

432

433 **Fig. 4: NMS-873 inhibits translocation by locking the ISS motif.**

434 **a,** Chemical structure of NMS-873. **b,** Sample preparation procedures. Steps performed at 4 °C

435 are in blue boxes. Steps performed at room temperature are in red boxes. **c,** Cryo-EM maps

436 and models of human p97 in complex with NMS-873. The maps and models are aligned.

437 Contour level: unsharpened map, 0.018; sharpened map, 0.052. **d,** D2 domain of the complex

structure in panel **c**, with the NMS-873 binding site zoomed in. The density of NMS-873 and the interacting residues are shown as magenta and gray mesh, respectively. Contour level: 6.0 rmsd. **e,** A different view of the NMS-873 binding site, with side chains of interacting residues shown. Contour level: 6.0 rmsd. **f,** A comparison of nucleotide binding sites in NMS-873 bound, translocating (chain D in open state), and nontranslocating (PDB ID: 7JY5) structures. The bottom D2 domains (green, salmon, and gray) are aligned. **g,** Substrate unfolding assay for wild-type p97 in the presence of different concentrations of NMS-873. One p97 hexamer can bind 6 equivalents (eq) of NMS-873.

447 **FIG. 5**

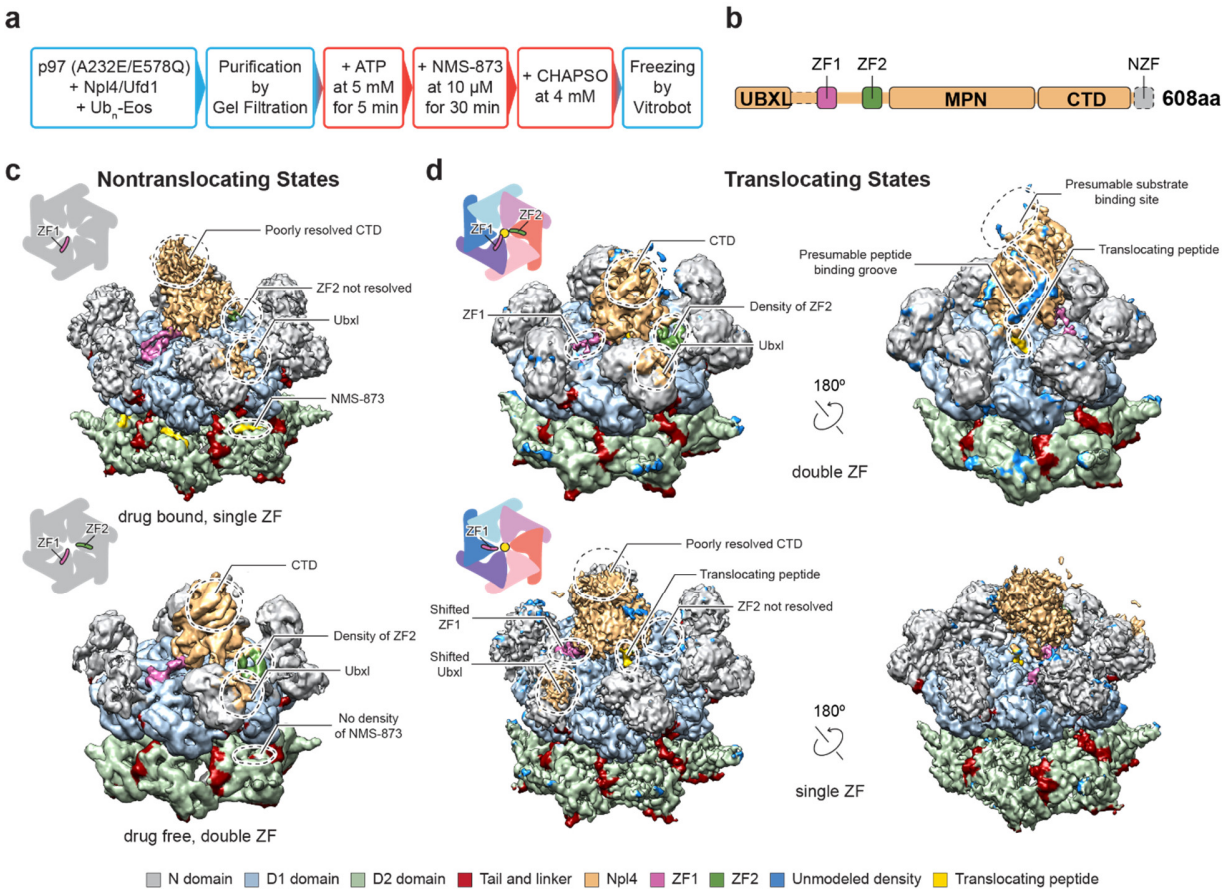

448

449 **Fig. 5: Conformational states of Npl4 in the presence of NMS873 at a substoichiometric**

450 **concentration.**

451 **a,** Sample preparation procedures. Steps performed at 4 °C are in blue boxes. Steps performed

452 at room temperature are in red boxes. **b,** Domain architecture of human Npl4. The color code of

453 the individual motifs are the same as that in panels **c** and **d**. Dotted parts are not resolved in the

454 cryo-EM maps. **c,** Two unsharpened cryo-EM maps in nontranslocating states resolved from the

455 dataset (**Extended Data Fig. 10**), one bound with NMS-873 (top). Contour level: 0.013. **d,** Two

456 unsharpened cryo-EM maps in translocating states resolved from the dataset. Contour level:

457 top, 0.01; bottom, 0.013. Different positions of zinc finger motifs of Npl4 are illustrated in the

458 insets.

459 **EXTENDED DATA Figures and Legends**

460 **EXTENDED DATA FIG. 1**

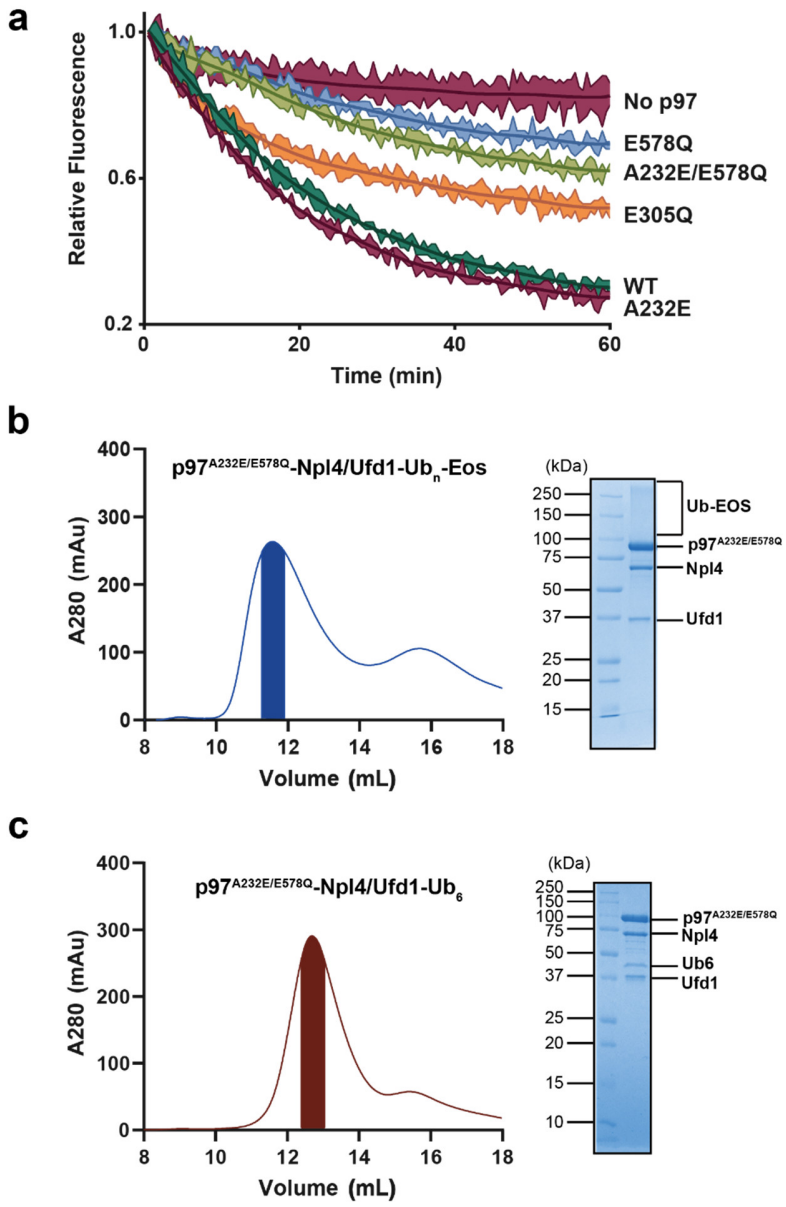

461

462 **Extended Data Fig. 1: Substrate unfolding activity of various p97 mutants and the**

463 **purification of cofactor- and substrate-engaged p97 complexes.**

464 **a,** Substrate unfolding assay for wild-type (WT) p97 and various mutations. E305Q and E578Q

465 are the two Walker B mutations in the D1 and D2 domains, respectively. A232E is a disease

466 mutation found in multisystem proteinopathy (MSP)[27,32]. **b,** Gel filtration chromatogram and

467 SDS-PAGE gel of the p97$^{A232E/E578Q}$-Npl4/Ufd1-Ub$_n$-Eos complex. **c,** Gel filtration chromatogram

468 and SDS-PAGE gel of the p97$^{A232E/E578Q}$-Npl4/Ufd1-Ub$_n$-Eos complex.

469 **EXTENDED DATA FIG. 2**

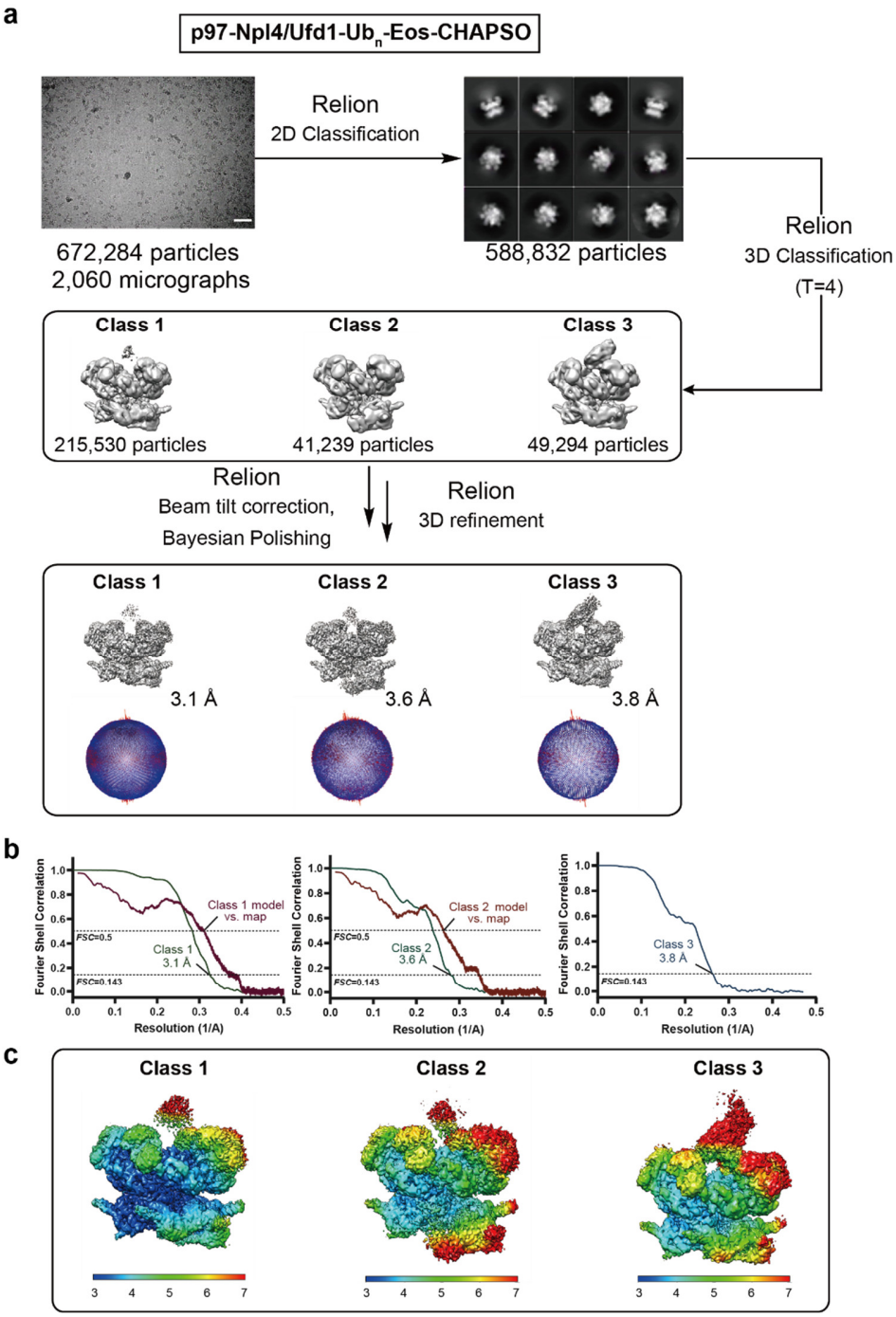

470

471 **Extended Data Fig. 2: Single-particle cryo-EM analyses for the p97-Npl4/Ufd1-Ub$_n$-Eos-**

472 **CHAPSO dataset.**

a, The workflow of data processing. The dataset was subjected to particle selection, 2D classification, and multiple rounds of 3D classification. A representative micrograph (scale bar corresponds to 50 nm) and representative 2D class averages are shown. Three classes were resolved from the dataset, including class 1 (closed state), class 2 (open state), and class 3 (similar to the closed state but with the Npl4 density). The distributions of the Euler angles for each reconstruction are shown below the maps. **b,** Fourier shell correlation (FSC) curves of the masked maps after Relion postprocessing. The resolutions were determined by the FSC=0.143 criterion. The model vs. map FSC curves are also shown for class 1 and class 2 (red). **c,** Local resolutions of the maps calculated using Relion.

483 **EXTENDED DATA FIG. 3**

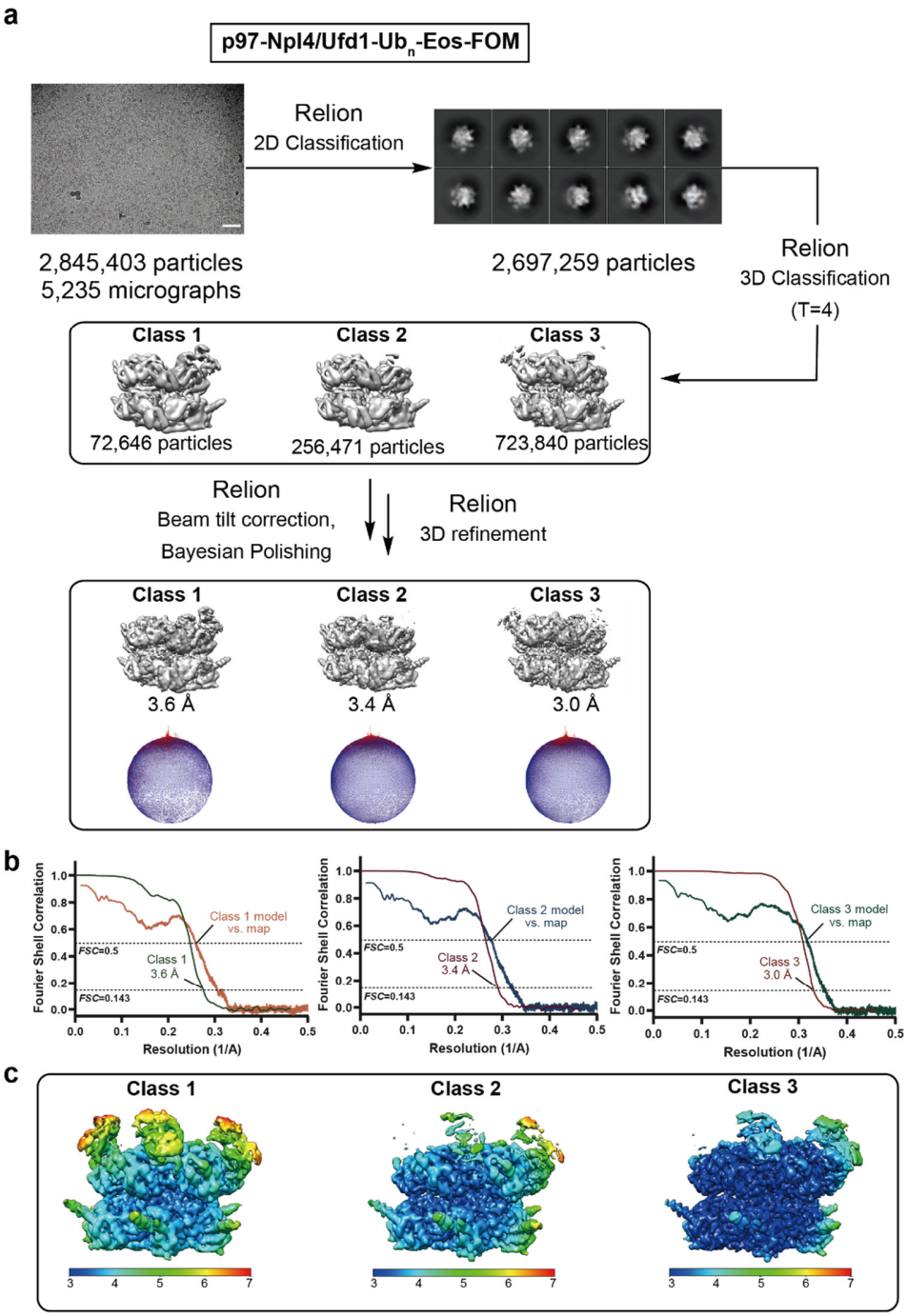

484

485 **Extended Data Fig. 3: Single-particle cryo-EM analyses for the p97-Npl4/Ufd1-Ub$_n$-Eos-**

486 **FOM dataset.**

a, The workflow of data processing. The dataset was subjected to particle selection, 2D classification, and multiple rounds of 3D classification. A representative micrograph (scale bar corresponds to 50 nm) and representative 2D class averages are shown. Three classes were resolved from the dataset. The distributions of the Euler angles for each reconstruction are shown below the maps. **b,** FSC curves of the masked maps after Relion postprocessing. The resolutions were determined by the FSC=0.143 criterion. The model vs. map FSC curves for each class are also shown. **c,** Local resolutions of the maps calculated using Relion.

495 **EXTENDED DATA FIG. 4**

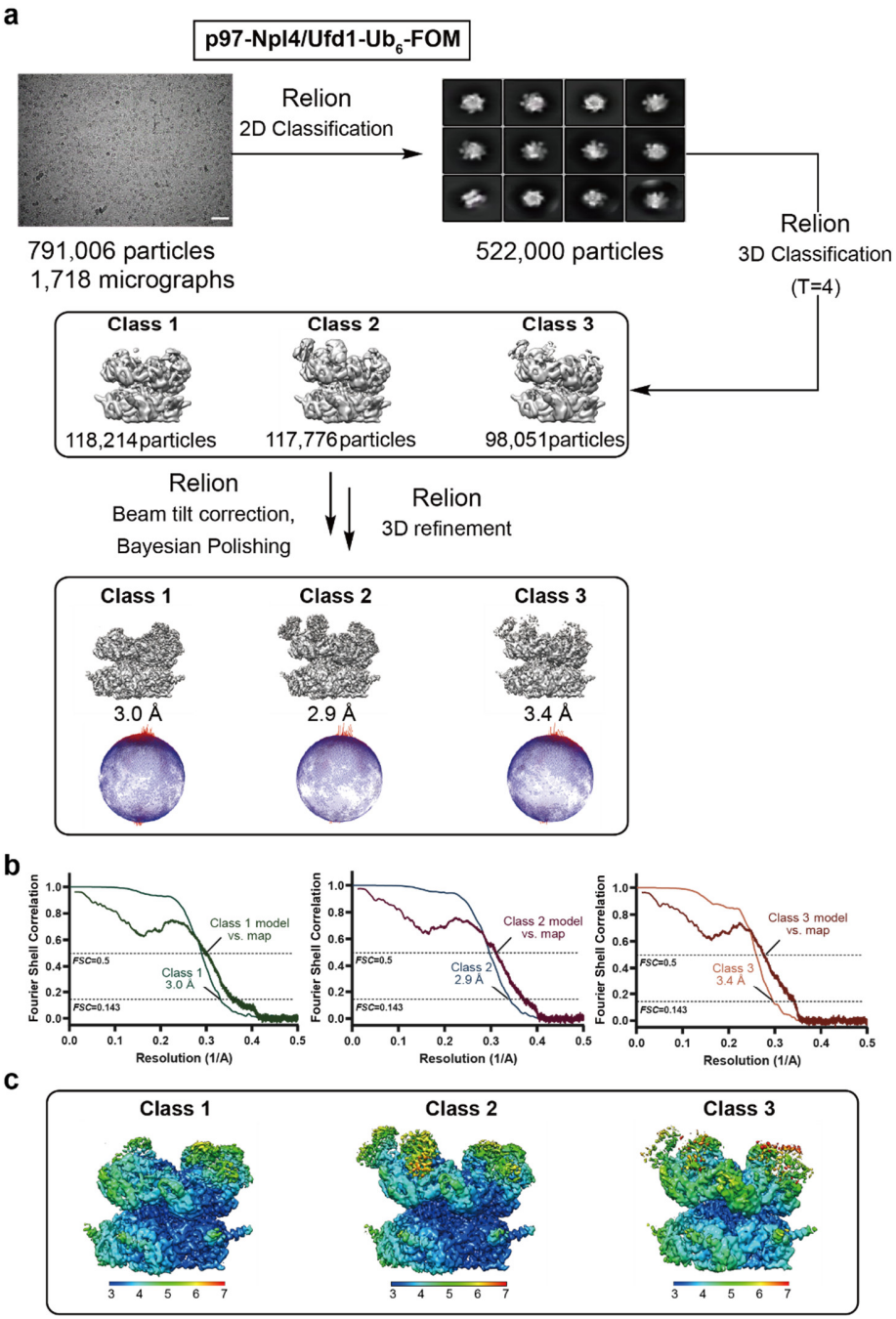

496

497 **Extended Data Fig. 4: Single-particle cryo-EM analyses for the p97-Npl4/Ufd1-Ub$_6$-FOM**

498 **dataset.**

499 **a,** The workflow of data processing. The dataset was subjected to particle selection, 2D

500 classification, and multiple rounds of 3D classification. A representative micrograph (scale bar

corresponds to 50 nm) and representative 2D class averages are shown. Three classes were resolved from the dataset. The distributions of the Euler angles for each reconstruction are shown below the maps. **b,** FSC curves of the masked maps after Relion postprocessing. The resolutions were determined by the FSC=0.143 criterion. The model vs. map FSC curves for each class are also shown. **c,** Local resolutions of the maps calculated using Relion.

507 **EXTENDED DATA FIG. 5**

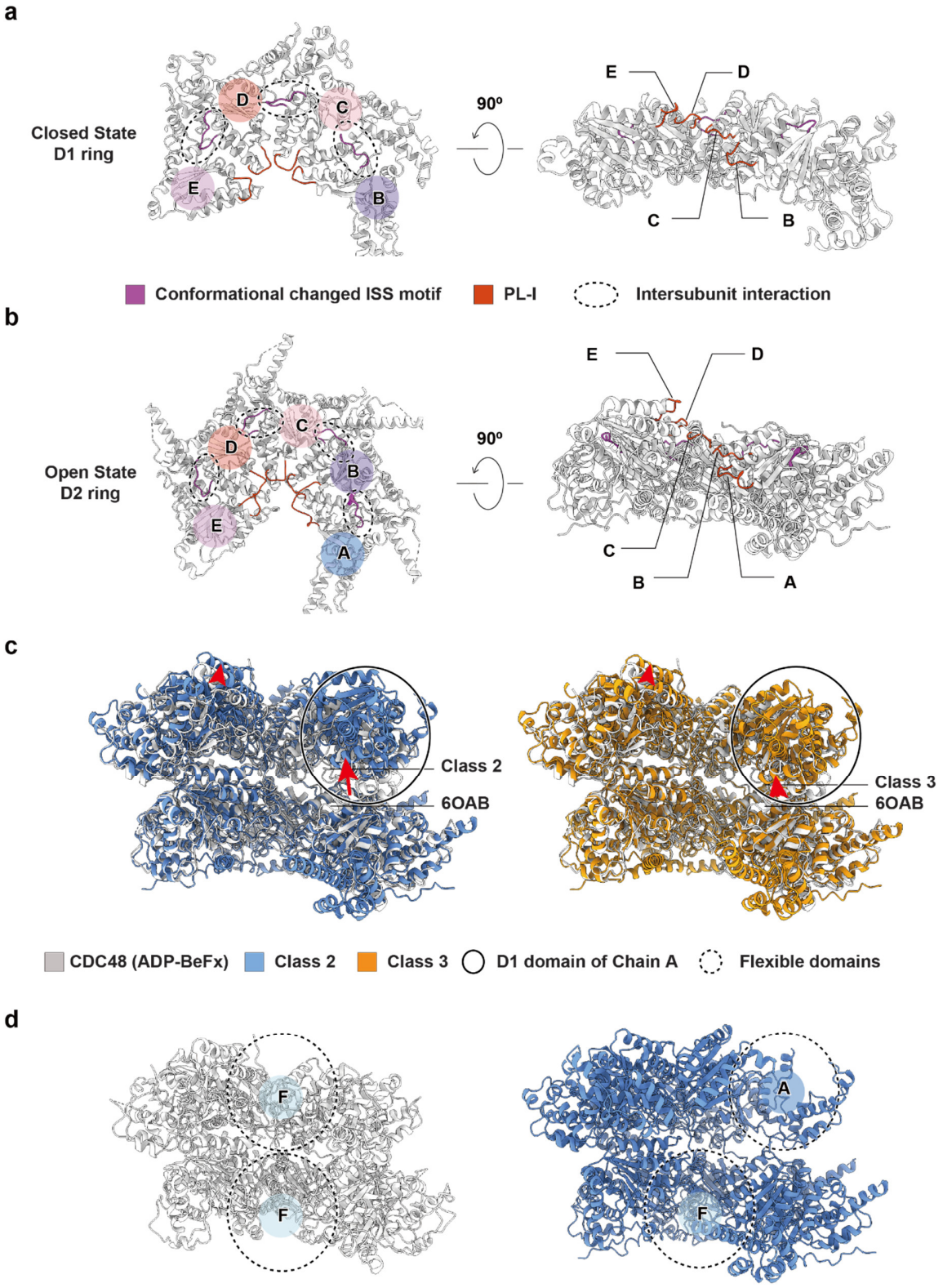

508

509 **Extended Data Fig. 5: Comparisons of human p97 and yeast Cdc48 structures.**

510 **a-b,** Illustrations showing the arrangement of chains B-E in the D1 ring of the closed state (**a**)
511 and chains A-E in the D2 ring of the open state (**b**). The labels of chains share the same color
512 code as in Fig. 1E. **c,** Comparisons of cryo-EM models of translocating structures of p97 (class
513 2, medium blue; class 3, orange) from the p97-Npl4/Ufd1-Ub_n-Eos-FOM dataset with Cdc48
514 (ADP-BeFx, PDB ID: 6OAB, light grey). The models were aligned based on the D2 ring. The
515 relative shifts of the D1 domain in chain A are noted by red arrows. **d,** Illustrations showing the
516 model of Cdc48 (ADP-BeFx, PDB ID: 6OAB, light grey, left panel) and the translocating
517 structure of p97 (class 2, medium blue, right panel) without the flexible domains. The entire
518 chain F in Cdc48 (ADP-BeFx) was flexible according to the previous publication [19]. The D2
519 domain in chain F and D1 domain in chain A were flexible in this study. Both (positioned in
520 dotted circles) were hid for comparison. Note that the staircases formed by D1 and D2 rings are
521 in register for Cdc48 and out of register for p97.

522

523 **EXTENDED DATA FIG. 6**

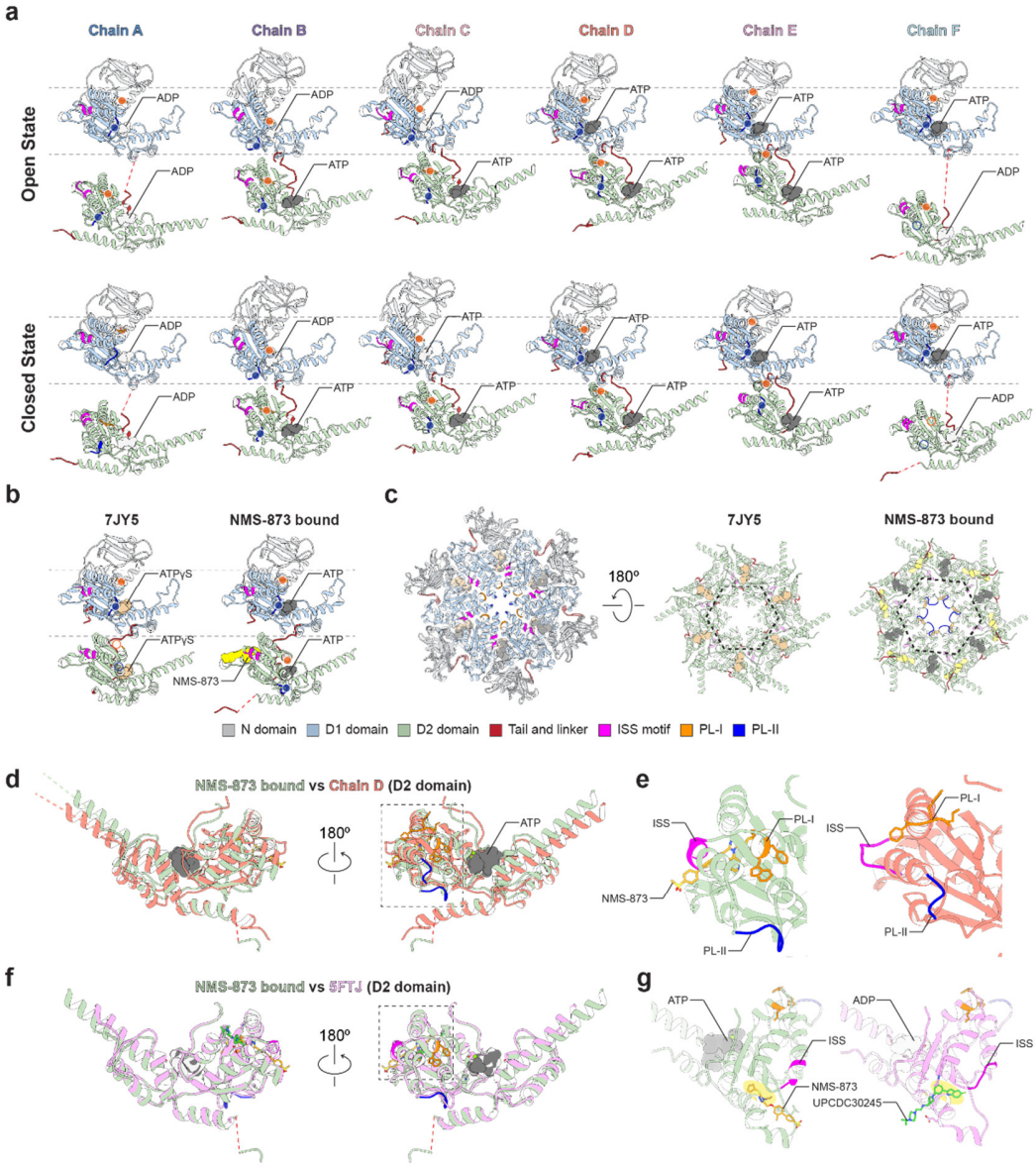

524

525 **Extended Data Fig. 6: Comparison of various p97 structures.**

526 **a,** Unrolling of the open (top row) and closed (bottom row) states of p97. The lateral and vertical
527 movement of D2 domains can be visualized. The positions of pore loops are marked with solid
528 dots. Unresolved pore loops are marked by open circles. **b,** Unrolling of the ATPγS-bound
529 nontranslocating structure (PDB ID: 7JY5) and NMS-873-bound structure. Only one chain of

each structure is shown since both structures are sixfold symmetric. **c,** A superimposition of 7JY5- and NMS-873-bound structures. Left: a top view of the N and D1 domains; Right: a bottom view of the D2 ring. The opening of the D2 ring is marked by a dotted hexagon. Panels **a, b,** and **c** share the same color code. **d,** A comparison of the D2 domain in the NMS-873-bound structure and that in chain D of the open state. The superimposition is based on the α/β subdomain. **e,** Magnified views of the dotted box in panel **d**, showing the conformations of the PL-I, PL-II, and ISS motifs. **f,** A comparison of the D2 domain in NMS-873- and UPCDC30245 (PDB ID: 5FTJ)-bound structures. The superimposition is based on the α/β subdomain. **g,** Magnified views of the dotted box in panel **f**, showing the binding sites of the compounds and the conformations of the ISS motif.

541 **EXTENDED DATA FIG. 7**

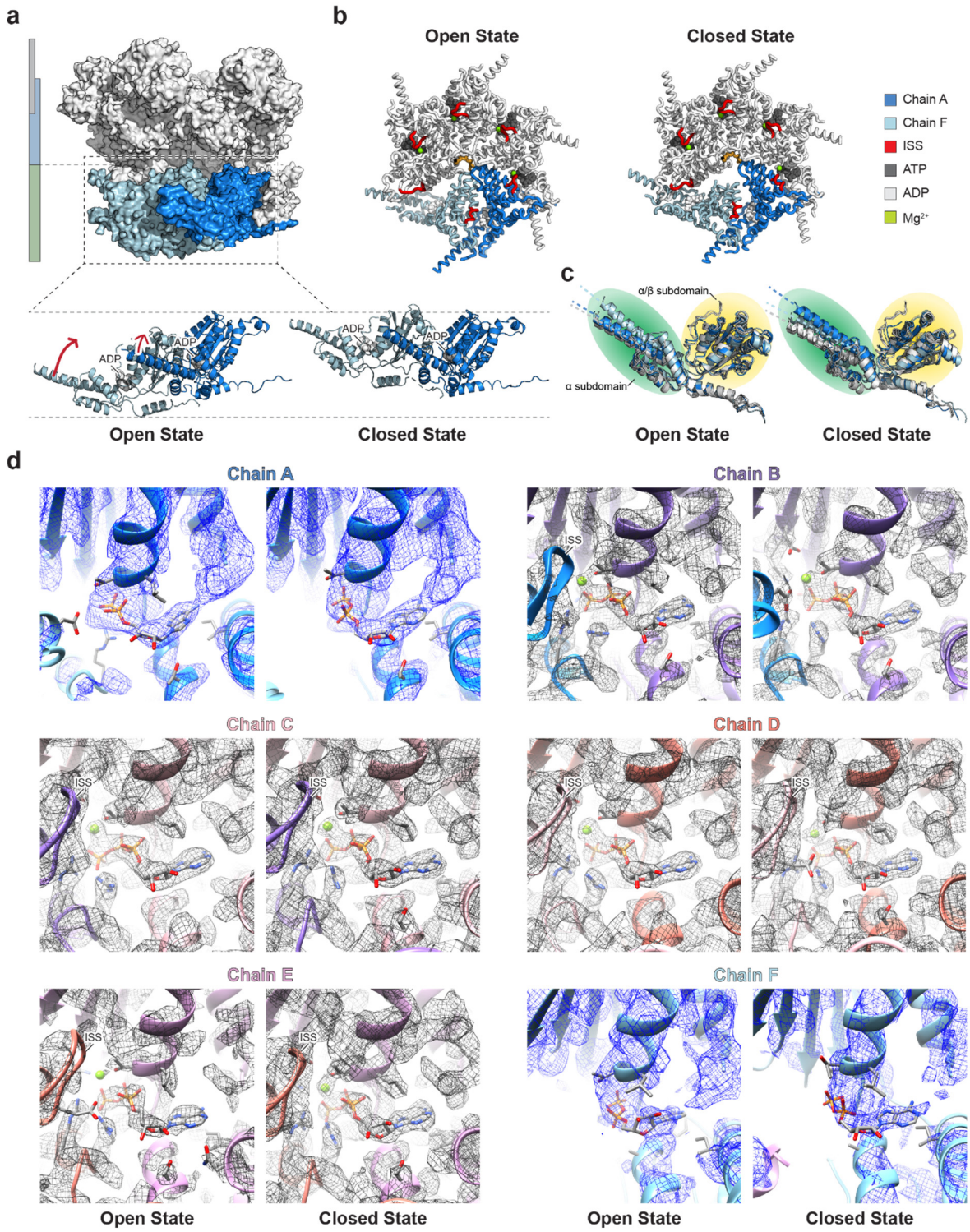

542

Extended Data Fig. 7: The power stroke motion and the nucleotide binding sites of the D2 domains.

a, A superimposition of the open and closed state structures, with two D2 domains (chain A and chain F) magnified. The relative positions of the D2 domains in chain A and chain F can be visualized. **b,** Top views of the D2 ring in the open and closed states, highlighting chain A, chain F, and the ISS motifs. **c,** Superimpositions of all D2 domains in the open and closed states based on the α/β subdomain. The directions of α7 helices are highlighted by dotted lines for comparison (dark blue, chain A; light blue, chain F; and gray, other chains). **d,** Individual nucleotide binding sites of the D2 domains in the open and closed states. Blue mesh: unsharpened map at contour level; Gray mesh: sharpened map at contour level.;

554 **EXTENDED DATA FIG. 8**

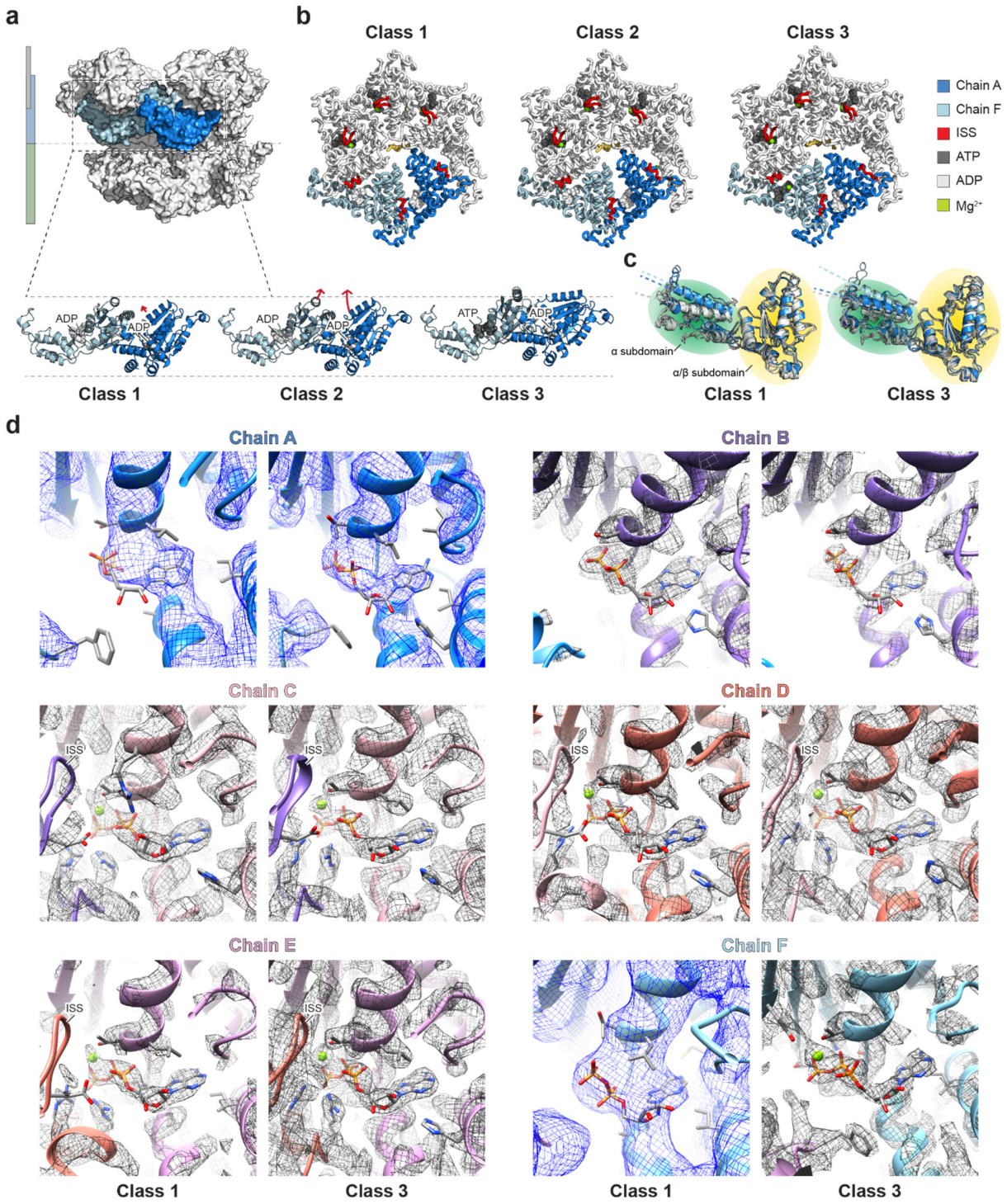

555

556 **Extended Data Fig. 8: The power stroke motion and the nucleotide binding sites of the D1**

557 **domains.**

558 **a,** A superimposition of three structures (classes 1, 2, and 3) from the p97-Npl4/Ufd1-Ub_n-Eos-
559 FOM dataset, with two D1 domains (chain A and chain F) magnified. The relative positions of
560 the D1 domains in chain A and chain F can be visualized. **b,** Top views of the D1 ring in the
561 three classes, highlighting chain A, chain F, and the ISS motifs. **c,** Superimpositions of all D1
562 domains in class 1 and class 3 based on the α/β subdomain. The directions of α7 helices are
563 highlighted by dotted lines for comparison (dark blue, chain A; light blue, chain F; and gray,
564 other chains). **d,** Individual nucleotide binding sites of the D1 domains in class 1 and class 3.
565 Blue mesh: Unsharpened map at contour level; Gray mesh: sharpened map at contour level.;
566

567 **EXTENDED DATA FIG. 9**

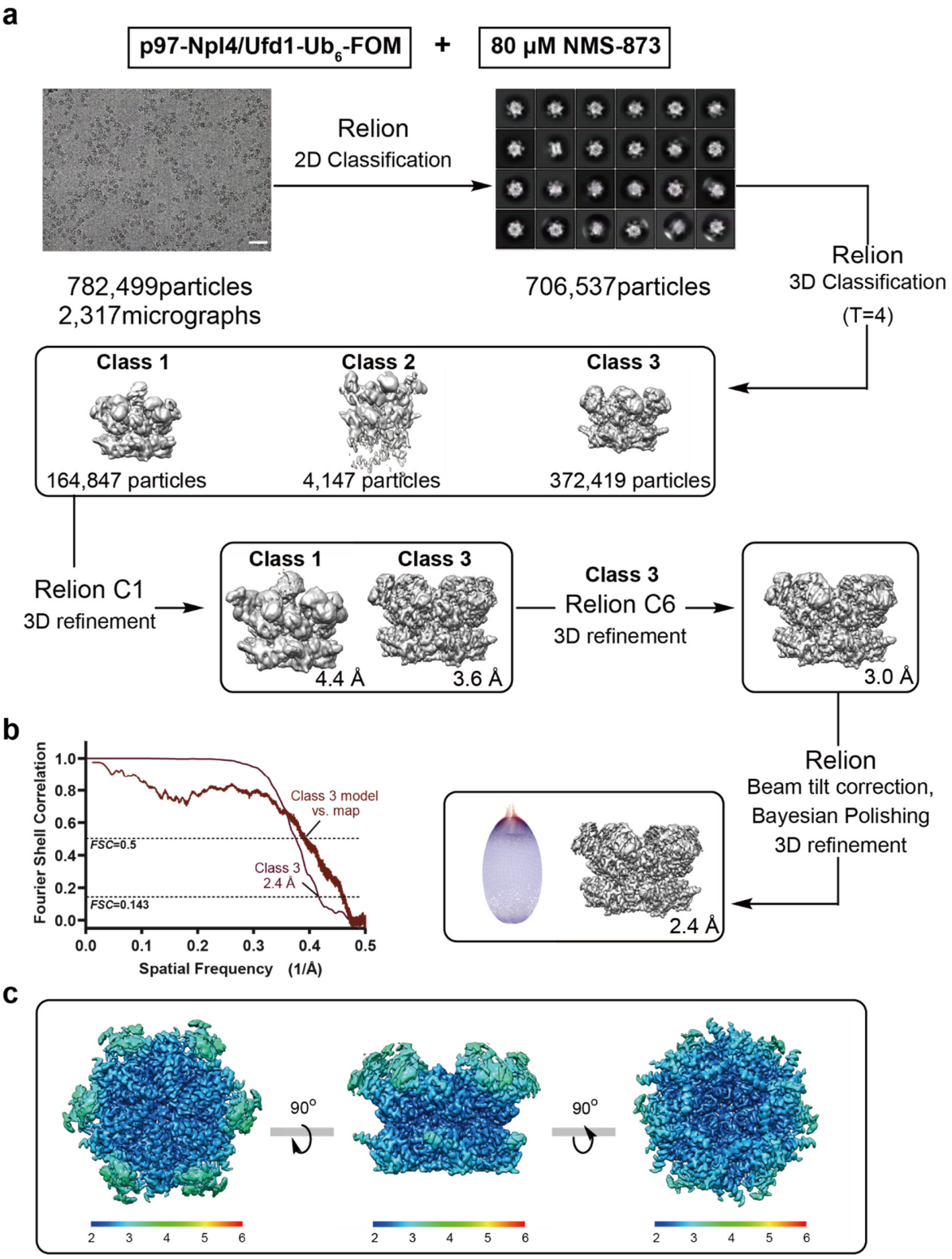

568

569 **Extended Data Fig. 9: Single-particle cryo-EM analyses for the p97-Npl4/Ufd1-Ub_6**
570 **complex in the presence of 80 μM NMS-873.**
571 **a,** The workflow of data processing. The dataset was subjected to particle selection, 2D
572 classification, and multiple rounds of 3D classification. A representative micrograph (scale bar
573 corresponds to 50 nm) and representative 2D class averages are shown. A single class was
574 resolved from the dataset. The distribution of the Euler angles is shown next to the map. **b,** The
575 FSC curve of the masked map after Relion postprocessing. The resolution was determined by
576 the FSC=0.143 criterion. The model vs. map FSC curve is also shown. **c,** Local resolution of the
577 map calculated using Relion.
578
579

580 **EXTENDED DATA FIG. 10**

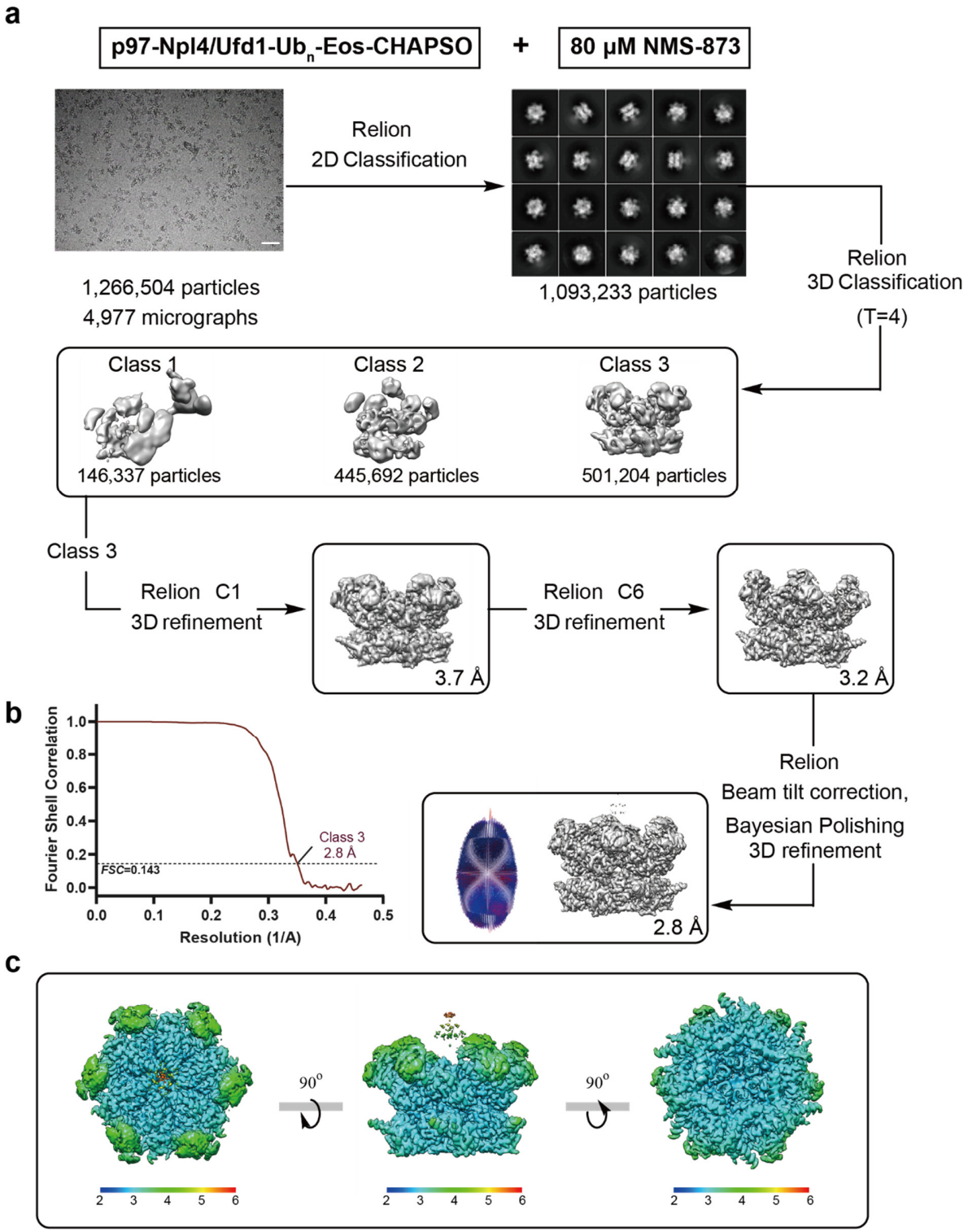

581

582 **Extended Data Fig. 10: Single-particle cryo-EM analyses for the p97-Npl4/Ufd1-Ub_n-Eos**
583 **complex in the presence of 80 μM NMS-873.**
584 **a,** The workflow of data processing. The dataset was subjected to particle selection, 2D
585 classification, and multiple rounds of 3D classification. A representative micrograph (scale bar
586 corresponds to 50 nm) and representative 2D class averages are shown. A single class was
587 resolved from the dataset. The distribution of the Euler angles is shown next to the map. **b,** The
588 FSC curve of the masked map after Relion postprocessing. The resolution was determined by
589 the FSC=0.143 criterion. **c,** Local resolution of the map calculated using Relion.
590
591
592

593 **EXTENDED DATA FIG. 11:**

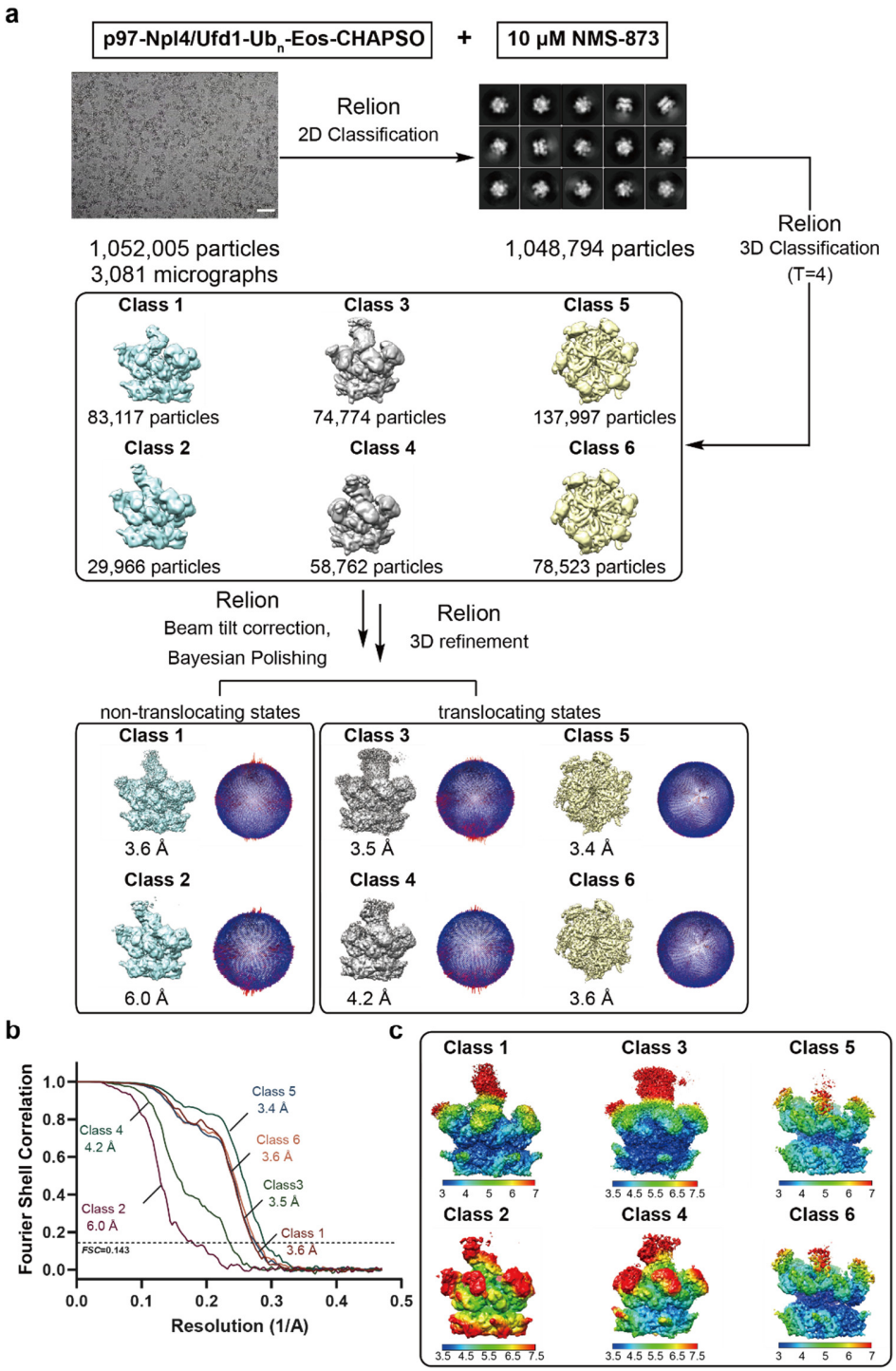

594

595 **Extended Data Fig. 11: Single-particle cryo-EM analyses for the p97-Npl4/Ufd1-Ub$_n$- Eos**

596 **complex in the presence of 10 μM NMS-873.**

a, The workflow of data processing. The dataset was subjected to particle selection, 2D classification, and multiple rounds of 3D classification. A representative micrograph (scale bar corresponds to 50 nm) and representative 2D class averages are shown. Six classes were resolved from the dataset, including two in nontranslocating states (Class 1 and Class 2) and four in translocating states (Class 3 through Class 6). The distributions of the Euler angles for each reconstruction are shown next to the maps. **b,** FSC curves of the masked maps after Relion postprocessing. The resolutions were determined by the FSC=0.143 criterion. **c,** Local resolutions of the maps calculated using Relion.

609 **Extended Data Table 1: Statistics of cryo-EM data collection and processing**

	p97-Npl4/Ufd1-Ub$_n$-Eos			**p97-Npl4/Ufd1-Ub$_n$-Eos**		
Detergent	CHAPSO (4 mM)			FOM (0.001%)		
Microscope	Krios (UChicago)			Krios (NCI)		
Magnification	81,000			81,000		
Voltage (kV)	300			300		
Spherical aberration (mm)	2.7			2.7		
Detector	K3			K3		
Camera mode	Super resolution counting			Super resolution counting		
Exposure rate (e^-/pixel/s)	15			15		
Total exposure (e^-/Å^2)	50			50		
Defocus range (μm)	-1.0 to -2.5			-1.0 to -2.5		
Pixel size (Å)	1.063			1.0794		
Mode of data collection	Image shift			Image shift		
Energy filter	20 eV slit			20 eV slit		
Software for data collection	EPU			Latitude S		
Number of micrographs	2,060			5,235		
Symmetry imposed	C1			C1		
Box size (pixel)	320			320		
Initial particle images (no.)	672,284			2,845,403		
Particle images for 3D (no.)	588,832			2,697,259		
	Class 1	Class 2	Class 3	Class 1	Class 2	Class 3
Final particle images (no.)	215,530	41,239	49,294	72,646	256,471	723,840
Map resolution, masked (Å)	3.09	3.58	3.77	3.63	3.45	3.02
B-factor estimated (Å^2)	79.7	79.7	80.3	97.6	109	96.8
EMD accession code	23449	23450	23451	23446	23447	23448

610

	p97-Npl4/Ufd1-Ub$_6$		
Detergent	FOM (0.001%)		
Microscope	Krios (UChicago)		
Magnification	81,000		
Voltage (kV)	300		
Spherical aberration (mm)	2.7		
Detector	K3		
Camera mode	Super resolution counting		
Exposure rate (e^-/pixel/s)	15		
Total exposure (e^-/Å^2)	50		
Defocus range (μm)	-1.0 to -2.5		
Pixel size (Å)	1.063		
Mode of data collection	Image shift		
Energy filter	20 eV slit		
Software for data collection	EPU		
Number of micrographs	1,718		
Symmetry imposed	C1		
Box size (pixel)	320		
Initial particle images (no.)	791,006		
Particle images for 3D (no.)	522,000		
	Class 1	Class 2	Class 3
Final particle images (no.)	118,214	117,776	98,051
Map resolution, masked (Å)	3.06	2.98	3.40
B-factor estimated (Å^2)	69.1	64.7	77.3
EMD accession code	23443	23444	23445

611
612

	p97-Npl4/Ufd1-Ub_6-NMS-873 (80 μM)	**p97-Npl4/Ufd1-Ub_n-Eos-NMS-873 (80 μM)**
Detergent	FOM (0.001%)	CHAPSO (4 mM)
Microscope	Krios (UChicago)	Krios (NCI)
Magnification	81,000	81,000
Voltage (kV)	300	300
Spherical aberration (mm)	2.7	2.7
Detector	K3	K3
Camera mode	Super resolution counting	Super resolution counting
Exposure rate (e^-/pixel/s)	15	15
Total exposure (e^-/Å^2)	50	50
Defocus range (μm)	-1.0 to -2.5	-1.0 to -2.5
Pixel size (Å)	1.063	1.0794
Mode of data collection	Image shift	Image shift
Energy filter	20 eV slit	20 eV slit
Software for data collection	EPU	Latitude S
Number of micrographs	2,317	4,977
Symmetry imposed	C6	C6
Box size (pixel)	320	320
Initial particle images (no.)	782,499	1,266,504
Particle images for 3D (no.)	706,537	1,093,233
Final particle images (no.)	372,419	501,204
Map resolution, masked (Å)	2.41	2.87
B-factor estimated (Å^2)	58.8	96.2
EMD accession code	23442	23452

613
614

	p97-Npl4/Ufd1-Ub$_n$-Eos-NMS-873 (10 µM)					
Detergent	CHAPSO (4 mM)					
Microscope	Krios (UChicago)					
Magnification	81,000					
Voltage (kV)	300					
Spherical aberration (mm)	2.7					
Detector	K3					
Camera mode	Super resolution counting					
Exposure rate (e^-/pixel/s)	15					
Total exposure (e^-/Å^2)	50					
Defocus range (µm)	-1.0 to -2.5					
Pixel size (Å)	1.063					
Mode of data collection	Image shift					
Energy filter	20 eV slit					
Software for data collection	Latitude S					
Number of micrographs	3081					
Symmetry imposed	C1					
Box size (pixel)	320					
Initial particle images (no.)	1,052,005					
Particle images for 3D (no.)	1,048,794					
	Non-Translocating		Translocating			
	Class 1	Class 2	Class 3	Class 4	Class 5	Class 6
Final particle images (no.)	83,317	29,966	74,774	58,762	137,997	78,523
Map resolution, masked (Å)	3.69	6.07	3.58	4.25	3.47	3.65
B-factor estimated (Å^2)	105	198	93.0	129	91.7	92.0
EMD accession code	23453	23454	23455	23456	23457	23458

615
616

617 **Extended Data Table 2: Statistics of cryo-EM model refinement and geometry**
618

Dataset: p97-Npl4/Ufd1-Ub$_n$-Eos-CHAPSO		
	Class1 (Closed State)	**Class2 (Open State)**
Composition (#)		
Chains	8	8
Atoms	35,051	35,072
Residues	Protein: 4,447	Protein: 4,456
Water	0	0
Ligands	MG: 7	MG: 7
	ADP: 5	ADP: 5
	ATP: 7	ATP: 7
Bonds (RMSD)		
Length (Å)	0.003	0.004
Angles (°)	0.617	0.673
MolProbity score	1.52	1.68
Clash score	9.95	10.93
Ramachandran plot (%)		
Outliers	0.00	0.02
Allowed	1.54	2.63
Favored	98.46	97.35
Rotamer outliers (%)	0.03	0.03
Cβ outliers (%)	0.00	0.00
Peptide plane (%)		
Cis proline/general	10.1/0.0	10.2/0.0
Twisted proline/general	0.0/0.0	0.0/0.0
CaBLAM outliers (%)	1.83	1.58
ADP (B-factors)		
Iso/Aniso (#)	35,051/0	35072/0
min/max/mean		
Protein	0.48/75.21/37.58	0.36/49.31/19.03
Ligand	11.67/65.09/33.22	2.26/41.30/13.85
PDB accession code	7LN5	7LN6

619
620

Dataset: p97-Npl4/Ufd1-Ub$_n$-Eos-FOM			
	Class1	**Class2**	**Class3**
Composition (#)			
Chains	8	8	8
Atoms	34,941	34,920	35,103
Residues	Protein: 4,433	Protein: 4,431	Protein: 4,455
Water	0	0	0
Ligands	MG: 7	MG: 7	MG: 8
	ADP: 5	ADP: 5	ADP: 4
	ATP: 7	ATP: 7	ATP: 8
Bonds (RMSD)			
Length (Å)	0.004	0.005	0.003
Angles (°)	0.651	0.674	0.604
MolProbity score	1.57	1.55	1.43
Clash score	11.31	10.70	7.52
Ramachandran plot (%)			
Outliers	0.07	0.07	0.00
Allowed	1.61	1.75	2.07
Favored	98.32	98.18	97.93
Rotamer outliers (%)	0.00	0.00	0.03
Cβ outliers (%)	0.00	0.00	0.00
Peptide plane (%)			
Cis proline/general	8.5/0.0	8.5/0.0	10.1/0.0
Twisted proline/general	0.0/0.0	0.0/0.0	0.0/0.0
CaBLAM outliers (%)	1.58	1.65	1.48
ADP (B-factors)			
Iso/Aniso (#)	34,941/0	34,920/0	35,103/0
min/max/mean			
Protein	0.79/73.39/37.41	0.45/71.85/36.71	0.39/86.71/50.32
Ligand	7.76/90.54/36.11	7.16/72.98/34.80	15.72/92.31/44.90
PDB accession code	7LN2	7LN3	7LN4

Dataset: p97-Npl4/Ufd1-Ub_6-FOM			
	Class1	**Class2**	**Class3**
Composition (#)			
Chains	8	8	8
Atoms	34,994	34,983	34,796
Residues	Protein: 4,434	Protein: 4,434	Protein:
Water	0	0	0
Ligands	MG: 8	MG: 7	MG: 7
	ADP: 4	ADP: 4	ADP: 5
	ATP: 8	ATP: 8	ATP: 7
Bonds (RMSD)			
Length (Å)	0.004	0.003	0.006
Angles (°)	0.654	0.646	0.759
MolProbity score	1.60	1.59	1.79
Clash score	12.30	11.95	14.43
Ramachandran plot (%)			
Outliers	0.09	0.05	0.05
Allowed	1.64	1.75	2.63
Favored	98.27	98.20	97.32
Rotamer outliers (%)	0.00	0.03	0.00
Cβ outliers (%)	0.00	0.00	0.00
Peptide plane (%)			
Cis proline/general	8.9/0.0	8.9/0.0	9.0/0.0
Twisted proline/general	0.0/0.0	0.0/0.0	0.0/0.0
CaBLAM outliers (%)	1.60	1.67	
ADP (B-factors)			
Iso/Aniso (#)	34,994/0	34,983/0	34,796/0
min/max/mean			
Protein	3.48/79.40/39.29	2.27/77.11/40.21	2.28/70.59/33.60
Ligand	12.21/68.94/37.64	8.22/74.08/36.83	11.82/52.39/30.60
PDB accession code	7LMZ	7LN0	7LN1

623

Dataset: p97-Npl4/Ufd1-Ub$_6$-NMS-873 (80 µM)	
Composition (#)	
Chains	6
Atoms	35,646
Residues	Protein: 4,470
Water	0
Ligands	MG: 12
	NM3: 6 (NMS-873)
	ATP: 6
Bonds (RMSD)	
Length (Å)	0.003 (0)
Angles (°)	0.845 (3)
MolProbity score	1.79
Clash score	8.11
Ramachandran plot (%)	
Outliers	0.00
Allowed	2.71
Favored	97.29
Rotamer outliers (%)	1.89
Cβ outliers (%)	0.00
Peptide plane (%)	
Cis proline/general	10.0/0.0
Twisted proline/general	0.0/0.0
CaBLAM outliers (%)	0.95
ADP (B-factors)	
Iso/Aniso (#)	35,646/0
min/max/mean	
Protein	1.58/57.10/22.25
Ligand	2.92/28.45/15.85
PDB accession code	7LMY

626 **Table S3: A summary of human p97 disease mutations and potentially affected**
627 **structures**
628

Disease Mutations	Potentially Affected Structures
R93C/R93H, I114V, I151V	N domain structure
I126F, T127A, P137L, M158V, R159G/R159C/R159H, E185K	N-cofactor interaction
I27V, R95C/R95G/R95H, G97E, R155S/R155H/R155L, G156C/G156S, G157R, M158V, R159G/R159C/R159H, R191G/R191Q, L198W, G202W, A232E, T262A, K386E, N387H/N387S/N387T, A439S/A439P/A439G	N-D1 interaction
I206F	D1 nucleotide binding site
A232E	D1-D1 interaction
D395G	D1 domain structure
N401S	D1-D2 interaction
R487H, R662C	D2-D2 interaction
D592N	Pore loop II of D2 domain
N750S	C terminal tail

629

630 **STAR METHODS**

631 **Data and code availability**

632 Cryo-EM maps have been deposited in the Electron Microscopy Data Bank (EMDB,
633 www.ebi.ac.uk/pdbe/emdb/) under the accession codes EMDB-23449 (p97-Npl4/Ufd1-Ub_n-Eos-
634 CHAPSO, Class 1), EMDB-23450 (p97-Npl4/Ufd1-Ub_n-Eos-CHAPSO, Class 2), EMDB-23451
635 (p97-Npl4/Ufd1-Ub_n-Eos-CHAPSO, Class 3), EMDB-23446 (p97-Npl4/Ufd1-Ub_n-Eos-FOM,
636 Class 1), EMDB-23447 (p97-Npl4/Ufd1-Ub_n-Eos-FOM, Class 2), EMDB-23448 (p97-Npl4/Ufd1-
637 Ub_n-Eos-FOM, Class 3), EMDB-23443 (p97-Npl4/Ufd1-Ub_6 -FOM, Class 1), EMDB-23444 (p97-
638 Npl4/Ufd1-Ub_6-FOM, Class 2), EMDB-23445 (p97-Npl4/Ufd1-Ub_6-FOM, Class 3), EMDB-23442
639 (p97-Npl4/Ufd1-Ub_6-NMS-873-FOM), EMDB-23452 (p97-Npl4/Ufd1-Ub_n-Eos-NMS-873-
640 CHAPSO), EMDB-23453 (p97-Npl4/Ufd1-Ub_n-Eos-NMS-873(substoichiometric)-CHAPSO,
641 Class 1), EMDB-23454 (p97-Npl4/Ufd1-Ub_n-Eos-NMS-873(substoichiometric)-CHAPSO, Class
642 2), EMDB-23455 (p97-Npl4/Ufd1-Ub_n-Eos-NMS-873(substoichiometric)-CHAPSO, Class 3),
643 EMDB-23456 (p97-Npl4/Ufd1-Ub_n-Eos-NMS-873(substoichiometric)-CHAPSO, Class 4),
644 EMDB-23457 (p97-Npl4/Ufd1-Ub_n-Eos-NMS-873(substoichiometric)-CHAPSO, Class 5),
645 EMDB-23458 (p97-Npl4/Ufd1-Ub_n-Eos-NMS-873(substoichiometric)-CHAPSO, Class 6). The
646 atomic models have been deposited in the Protein Data Bank (PDB, www.rcsb.org) under the
647 accession codes 7LN5 (p97-Npl4/Ufd1-Ub_n-Eos-CHAPSO, Class 1), 7LN6 (p97-Npl4/Ufd1-Ub_n-
648 Eos-CHAPSO, Class 2), 7LN2 (p97-Npl4/Ufd1-Ub_n-Eos-FOM, Class 1), 7LN3 (p97-Npl4/Ufd1-
649 Ub_n-Eos-FOM, Class 2), 7LN4 (p97-Npl4/Ufd1-Ub_n-Eos-FOM, Class 3), 7LMZ (p97-Npl4/Ufd1-
650 Ub_6 -FOM, Class 1), 7LN0 (p97-Npl4/Ufd1-Ub_6-FOM, Class 2), 7LN1 (p97-Npl4/Ufd1-Ub_6-FOM,
651 Class 3), 7LMY (p97-Npl4/Ufd1-Ub_6-NMS-873-FOM).

652

653 **Protein expression and purification**

654 Wildtype human p97, human p97 mutants, Npl4/Ufd1, His_6-Ub^{G76V}-Ub^{G76V}-mEos3.2 (Ub-
655 Eos), human UBA1, Ube25k and gp78RING-Ube2g2 were purified as previously

656 described[26,32,37]. Briefly, all proteins were expressed in *E. coli* BL21(DE3) cells and purified
657 through Ni-NTA resin at 4 °C. All purified proteins were further buffer-exchanged to the Storage
658 Buffer containing 50 mM HEPES, pH 8.0, 150 mM NaCl, 1 mM $MgCl_2$, 0.5 mM tris(2-
659 carboxyethyl)phosphine (TCEP) before snap freezing.
660
661 **Preparation of polyubiquitinated Ub-Eos and polyubiquitin chain**
662 For cryo-EM studies, His-tagged Ub-Eos was directly used for polyubiquitination. For the
663 substrate unfolding assay, Ub-Eos was first irradiated under LED UV light (385-395 nm,
664 uvBeast V2) for 1 hour at 4 ºC to induce the photoconversion of mEos3.2, followed by
665 polyubiquitination. The polyubiquitination reaction was performed as previously described[32].
666 Briefly, 20 μM Ub-Eos was mixed with 1 μM UBA1, 20 μM gp78RING-Ube2g2, and 500 μM
667 ubiquitin in the Ubiquitination Buffer containing 20 mM Hepes, pH 7.4, 150mM KCl, 10 mM ATP,
668 and 10 mM $MgCl_2$. After incubation at 37 ºC overnight, the mixture was incubated with Ni-NTA
669 resin to remove free ubiquitin chains. The elution was further separated using a Superdex 200
670 (GE Healthcare) size-exclusion column equilibrated in the Storage Buffer. Polyubiquitinated Ub-
671 Eos (Ub_n-Eos) with longer ubiquitin chains (estimated over 10 ubiquitin subunits) was collected
672 and flash frozen for the substrate unfolding assay.
673 K48-linked polyubiquitin chains were assembled by mixing 1 μM UBA1, 10 μM Ube25k,
674 and 1 mM ubiquitin in the Ubiquitination Buffer at 37 ºC for 4 hours. The reaction mixture was
675 then diluted 10 folds with 50 mM NaOAc, pH 4.5, and separated by a Mono S cation exchange
676 column. The corresponding peak for hexa-ubiquitin chain (Ub_6) was collected and further
677 purified with a Superdex 75 (GE Healthcare) size-exclusion column equilibrated in the Storage
678 Buffer.
679
680 **Assembly of substrate-engaged p97 complex**

681 p97-Npl4/Ufd1 complex was assembled as previously described[26]. A p97 mutant bearing
682 A232E and E578Q mutations was used in order to decrease the heterogeneity of N domains
683 and reduce the unfolding activity of the complex. Two-fold molar excess of Ub_6 or Ub_n-Eos was
684 added to the p97-Npl4/Ufd1 complex, followed by gel filtration using a Superose 6 column (GE
685 Healthcare) equilibrated in the Storage Buffer (**Extended Data Fig. 1b and 1c**). The assembled
686 substrate-engaged p97 complex was flash frozen in liquid nitrogen for structural studies. No
687 nucleotide was supplemented during the assembly.
688
689 **Specimen preparation for single-particle cryo-EM**
690 All samples for cryo-EM were prepared as previously described[26], with the following
691 modifications. Either fluorinated octyl maltoside (FOM) or CHAPSO was used to relieve the
692 preferred orientations instead of IGEPAL CA-630. The complex was concentrated to ~2.5
693 mg/mL followed by incubation with 5 mM ATP at room temperature for 5 minutes before adding
694 FOM (final concentration 0.01% v/v). Glow discharged Quantifoil Cu 1.2/1.3 grids were used for
695 FOM supplemented samples. Alternatively, the samples were concentrated to ~20mg/mL
696 followed by incubation with 5 mM ATP at room temperature for 5 minutes before adding
697 CHAPSO (final concentration 4 mM). Non-glow-discharged Quantifoil Cu 1.2/1.3 grids were
698 used for CHAPSO supplemented samples. In both cases, 3.5 μL sample was applied to the grid
699 and was blotted for 1 second using standard Vitrobot filter paper (Ted Pella, 47000-100) before
700 plunge freezing in liquid ethane. For substrate-engaged p97-Npl4/Ufd1 complex in the presence
701 of NMS-873, besides the aforementioned procedures, NMS-873 was supplemented right after
702 the incubation with ATP at either 10 μM or 80 μM final concentration. The samples were
703 incubated for another 30 min at room temperature before adding the detergents and plunge
704 freezing.
705
706 **Data collection for single-particle cryo-EM**

707 Data collection was performed either in Advanced Electron Microscopy Facility at the
708 University of Chicago or National Cryo-Electron Microscopy Facility at the National Cancer
709 Institute. All datasets were acquired as movie stacks with a Titan Krios electron microscope
710 operating at 300 kV, equipped with either a Gatan K2 Summit or K3 direct detector camera. A
711 single stack typically consists of 40 frames with a total exposure around 50 electrons/$Å^2$. The
712 defocus range was set at -1.0 to -2.5 μm. See **Supplementary Table 1** for the details.
713
714 **Image processing**
715 Movie stacks were subjected to beam-induced motion correction using MotionCor2[38].
716 CTF parameters for each micrograph were determined using CTFFIND4[39]. Particle picking, two-
717 and three-dimensional classifications, three-dimensional refinement, and local resolution
718 estimation were performed in RELION-3[40]. Particle picking was performed by manually
719 choosing ~2,000 particles and generating templates through reference free 2D classification,
720 followed by automatic template based picking. False-positive particles or particles classified in
721 poorly defined classes were discarded after 2D classification. The initial 3D classification was
722 performed on a binned dataset with the previously reported p97 structures as the reference
723 model[26]. The detailed data processing flows are shown in Figures S2, 3, 4, 9, 10, and 11. To
724 make sure that the 3D classification did not miss any major conformations, additional runs were
725 performed with different number of classes (ranges from 3-8) and different regularization
726 parameters (ranges from 2-6). Since we did not observe a dependence on the regularization
727 parameter, the results from the default value (T=4) were shown in the figures. Data processing
728 statistics are summarized in **Supplementary Table 1**. Reported resolutions are based on
729 Fourier shell correlation (FSC) using the FSC=0.143 criterion.
730
731 **Model building, refinement, and validation**

732 Model building was based on the existing cryo-EM structures of human p97[26] (PDB ID:
733 7JY5). The models of individual domains (N, D1, and D2) were first docked into the cryo-EM
734 maps as rigid bodies using UCSF Chimera[41] followed by further adjustment using COOT[42]. For
735 well-resolved regions, sharpened maps were used and individual residues were manually
736 adjusted and fit into the density. For flexible regions, unsharpened maps were used and
737 individual secondary structure elements or subdomains were fit into the density as rigid bodies.
738 A short β strand was automatically built into the density corresponding to the translocating
739 peptide using COOT, followed by manual extension on either ends and real-space refinement
740 until the all the density was covered. The final models were subjected to global refinement and
741 minimization in real space using the real-space refinement module in Phenix[43]. Model validation
742 was performed using the comprehensive validation tool in Phenix. The statistics of model
743 refinement is shown in **Supplementary Table 2**.
744
745 **Substrate unfolding assay**
746 Substrate unfolding assay was performed as previously described[26,32]. Briefly, 20 nM
747 photoconverted polyubiquitinated Ub-Eos was mixed with 400 nM p97 or p97 mutants and 500
748 nM Npl4/Ufd1 in the Assay Buffer containing 50 mM Tris pH 7.4, 5 mM KCl, 20 mM $MgCl_2$, 1
749 mM EDTA, 0.5 mM TCEP, and 0.01% Triton. Proteins were pre-incubated in a 96-well plate
750 (Costar 3694) for 10 minutes at 37 °C before initiating the reaction by supplementing the ATP
751 regeneration mixture (5 mM ATP, 30 mM creatine phosphate, and 50 µg/mL creatine
752 phosphokinase). Fluorescence signal was monitored using a TECAN safire2 plate reader at 540
753 nm excitation and 580 nm emission wavelengths with 30 seconds intervals for 60 min. Each
754 reaction condition was repeated three times. Background fluorescence was measured by mixing
755 the same amount of substrate with 6 M guanidine-HCl and was subtracted from the average of
756 the experimental groups. Normalized fluorescence was plotted using GraphPad Prism 8.4.2.

757 **REFERENCES**

758 1. Bodnar, N. & Rapoport, T. Toward an understanding of the Cdc48/p97 ATPase.
759 *F1000Res* **6**, 1318 (2017).
760 2. Erzberger, J.P. & Berger, J.M. Evolutionary relationships and structural mechanisms of
761 AAA+ proteins. *Annu. Rev. Biophys. Biomol. Struct.* **35**, 93-114 (2006).
762 3. Rabouille, C., Levine, T.P., Peters, J.-M. & Warren, G. An NSF-like ATPase, p97, and
763 NSF mediate cisternal regrowth from mitotic golgi fragments. *Cell* **82**, 905-914 (1995).
764 4. van den Boom, J. & Meyer, H. VCP/p97-Mediated Unfolding as a Principle in Protein
765 Homeostasis and Signaling. *Mol. Cell* **69**, 182-194 (2018).
766 5. Ye, Y.H., Tang, W.K., Zhang, T. & Xia, D. A Mighty "Protein Extractor" of the Cell:
767 Structure and Function of the p97/CDC48 ATPase. *Front Mol. Biosci.* **4**(2017).
768 6. Tang, W.K. & Xia, D. Mutations in the Human AAA(+) Chaperone p97 and Related
769 Diseases. *Front Mol. Biosci* **3**, 79 (2016).
770 7. Darwich, N.F. et al. Autosomal dominant VCP hypomorph mutation impairs
771 disaggregation of PHF-tau. *Science* **370**(2020).
772 8. Huryn, D.M., Kornfilt, D.J.P. & Wipf, P. p97: An Emerging Target for Cancer,
773 Neurodegenerative Diseases, and Viral Infections. *J. Med. Chem.* **63**, 1892-1907 (2020).
774 9. Skrott, Z. et al. Alcohol-abuse drug disulfiram targets cancer via p97 segregase adaptor
775 NPL4. *Nature* **552**, 194-199 (2017).
776 10. Xia, D., Tang, W.K. & Ye, Y. Structure and function of the AAA+ ATPase p97/Cdc48p.
777 *Gene* **583**, 64-77 (2016).
778 11. Huyton, T. et al. The crystal structure of murine p97/VCP at 3.6 angstrom. *J. Struct. Biol.*
779 **144**, 337-348 (2003).
780 12. Davies, J.M., Brunger, A.T. & Weis, W.I. Improved structures of full-length p97, an AAA
781 ATPase: Implications for mechanisms of nucleotide-dependent conformational change.
782 *Structure* **16**, 715-726 (2008).
783 13. Banerjee, S. et al. 2.3 A resolution cryo-EM structure of human p97 and mechanism of
784 allosteric inhibition. *Science* **351**, 871-5 (2016).
785 14. Zhang, X. et al. Structure of the AAA ATPase p97. *Mol. Cell* **6**, 1473-84 (2000).
786 15. Ripstein, Z.A., Huang, R., Augustyniak, R., Kay, L.E. & Rubinstein, J.L. Structure of a
787 AAA + unfoldase in the process of unfolding substrate. *Elife* **6,** e25754 (2017).
788 16. Puchades, C. et al. Structure of the mitochondrial inner membrane AAA + protease
789 YME1 gives insight into substrate processing. *Science* **358**, 609-+ (2017).
790 17. Zhao, M.L. et al. Mechanistic insights into the recycling machine of the SNARE complex.
791 *Nature* **518**, 61-67 (2015).
792 18. Cooney, I. et al. Structure of the Cdc48 segregase in the act of unfolding an authentic
793 substrate. *Science* **365**, 502-505 (2019).
794 19. Twomey, E.C. et al. Substrate processing by the Cdc48 ATPase complex is initiated by
795 ubiquitin unfolding. *Science* **365,** eaax1033 (2019).
796 20. Alverez, C. et al. Allosteric Indole Amide Inhibitors of p97: Identification of a Novel Probe
797 of the Ubiquitin Pathway. *Acs Med. Chem. Lett.* **7**, 182-187 (2016).
798 21. Magnaghi, P. et al. Covalent and allosteric inhibitors of the ATPase VCP/p97 induce
799 cancer cell death. *Nat. Chem. Biol.* **9**, 548-U44 (2013).
800 22. Zhang, T., Midshra, P., Hay, B.A., Chan, D. & Guo, M. Valosin-containing protein
801 (VCP/p97) inhibitors relieve Mitofusin-dependent mitochondrial defects due to VCP
802 disease mutants. *Elife* **6,** e17834 (2017).
803 23. Zhang, J.T. et al. Identification of NMS-873, an allosteric and specific p97 inhibitor, as a
804 broad antiviral against both influenza A and B viruses. *Eur. J. Pharm. Sci.* **133**, 86-94
805 (2019).

24. Bojkova, D. et al. Proteomics of SARS-CoV-2-infected host cells reveals therapy targets. *Nature* **583**, 469-472 (2020).
25. Hao, Q. et al. A non-canonical role of the p97 complex in RIG-I antiviral signaling. *Embo J.* **34**, 2903-2920 (2015).
26. Pan, M. et al. Seesaw conformations of Npl4 in the human p97 complex and the inhibitory mechanism of a disulfiram derivative. *Nat Commun* **12**, 121 (2021).
27. Blythe, E.E., Gates, S.N., Deshaies, R.J. & Martin, A. Multisystem Proteinopathy Mutations in VCP/p97 Increase NPLOC4.UFD1L Binding and Substrate Processing. *Structure* **27**, 1820-1829 (2019).
28. Bodnar, N.O. & Rapoport, T.A. Molecular Mechanism of Substrate Processing by the Cdc48 ATPase Complex. *Cell* **169**, 722-735 (2017).
29. Monroe, N., Han, H., Shen, P.S., Sundquist, W.I. & Hill, C.P. Structural basis of protein translocation by the Vps4-Vta1 AAA ATPase. *Elife* **6,** e24487 (2017).
30. Yokom, A.L. et al. Spiral architecture of the Hsp104 disaggregase reveals the basis for polypeptide translocation. *Nat. Struct. Mol. Biol.* **23**, 830-837 (2016).
31. Hanzelmann, P. & Schindelin, H. Structural Basis of ATP Hydrolysis and Intersubunit Signaling in the AAA+ ATPase p97. *Structure* **24**, 127-139 (2016).
32. Blythe, E.E., Olson, K.C., Chau, V. & Deshaies, R.J. Ubiquitin- and ATP-dependent unfoldase activity of P97/VCP center dot NPLOC4 center dot UFD1L is enhanced by a mutation that causes multisystem proteinopathy. *Proc Natl Acad Sci USA.* **114**, E4380-E4388 (2017).
33. Song, C., Wang, Q. & Li, C.-C.H. ATPase Activity of p97-Valosin-containing Protein (VCP). *J. Biol. Chem.* **278**, 3648-3655 (2003).
34. Martin, A., Baker, T.A. & Sauer, R.T. Rebuilt AAA + motors reveal operating principles for ATP-fuelled machines. *Nature* **437**, 1115-1120 (2005).
35. Meyer, H. & Weihl, C.C. The VCP/p97 system at a glance: connecting cellular function to disease pathogenesis. *J. Cell Sci.* **127**, 3877-83 (2014).
36. Tan, D., Blok, N.B., Rapoport, T.A. & Walz, T. Structures of the double-ring AAA ATPase Pex1/Pex6 involved in peroxisome biogenesis. *FEBS J.* **283**, n/a-n/a (2015).
37. Pickart, C.M. & Raasi, S. Controlled synthesis of polyubiquitin chains. *Methods Enzymol*. **399**, 21-36 (2005).
38. Zheng, S.Q. et al. MotionCor2: anisotropic correction of beam-induced motion for improved cryo-electron microscopy. *Nat. Methods* **14**, 331-332 (2017).
39. Mindell, J.A. & Grigorieff, N. Accurate determination of local defocus and specimen tilt in electron microscopy. *J. Struct. Biol.* **142**, 334-347 (2003).
40. Zivanov, J. et al. New tools for automated high-resolution cryo-EM structure determination in RELION-3. *Elife* **7,** e42166 (2018).
41. Pettersen, E.F. et al. UCSF chimera - A visualization system for exploratory research and analysis. *J. Comput. Chem.* **25**, 1605-1612 (2004).
42. Emsley, P. & Cowtan, K. Coot: model-building tools for molecular graphics. *Acta. Crystallogr. D.* **60**, 2126-2132 (2004).
43. Adams, P.D. et al. PHENIX: a comprehensive Python-based system for macromolecular structure solution. *Acta. Crystallogr. D.* **66**, 213-221 (2010).